

# The *Fermi* GBM Gamma-Ray Burst Spectral Catalog: The First Two Years

Adam Goldstein<sup>1</sup>, J. Michael Burgess<sup>1</sup>, Robert D. Preece<sup>1</sup>, Michael S. Briggs<sup>1</sup>, Sylvain Guiriec<sup>1</sup>, Alexander J. van der Horst<sup>2</sup>, Valerie Connaughton<sup>1</sup>, Colleen A. Wilson-Hodge<sup>3</sup>, William S. Paciesas<sup>1</sup>, Charles A. Meegan<sup>2</sup>, Andreas von Kienlin<sup>4</sup>, P. N. Bhat<sup>1</sup>, Elisabetta Bissaldi<sup>4</sup>, Vandiver Chaplin<sup>1</sup>, Roland Diehl<sup>4</sup>, Gerald J. Fishman<sup>3</sup>, Gerard Fitzpatrick<sup>5</sup>, Suzanne Foley<sup>4</sup>, Melissa Gibby<sup>6</sup>, Misty Giles<sup>6</sup>, Jochen Greiner<sup>4</sup>, David Gruber<sup>4</sup>, R. Marc Kippen<sup>7</sup>, Chryssa Kouveliotou<sup>3</sup>, Sheila McBreen<sup>5</sup>, Sinéad McGlynn<sup>8,4</sup>, Arne Rau<sup>4</sup>, and Dave Tierney<sup>5</sup>

## ABSTRACT

We present systematic spectral analyses of GRBs detected by the *Fermi* Gamma-Ray Burst Monitor (GBM) during its first two years of operation. This catalog contains two types of spectra extracted from 487 GRBs, and by fitting four different spectral models, this results in a compendium of over 3800 spectra. The models were selected based on their empirical importance to the spectral shape of many GRBs, and the analysis performed was devised to be as thorough and objective as possible. We describe in detail our procedure and criteria for the analyses, and present the bulk results in the form of parameter distributions. This catalog should be considered an official product from the *Fermi* GBM Science Team, and the data files containing the complete results are available from the High-Energy Astrophysics Science Archive Research Center (HEASARC).

*Subject headings:* gamma rays: bursts — methods: data analysis

## 1. Introduction

Compendia of physical observations of an enigmatic phenomenon such as Gamma-Ray Bursts (GRBs) should be as complete and uniform as possible,

so that useful inferences can be drawn from the assembled data. Here we have followed in a line of successful GRB Catalogs from the Burst And Transient Source Experiment (BATSE) to present the community with representative spectral fits for a complete sample of *Fermi* Gamma-Ray Burst Monitor (GBM) bursts, observed during the first two years of operation (July 14, 2008 to July 13, 2010). The methodology of producing this catalog strives to balance completeness, uniformity, and accuracy. The selection criteria, techniques, spectral models used for fitting, etc., all derive from a previous work, based upon BATSE data (Mallozzi et al. 1995), that is being prepared for publication as a complete sample from that earlier mission. It is our hope that the two data sets, the current GBM sample and the complete BATSE sample, can serve as a whole for comparison and contrast. Further, we will continue to add

<sup>1</sup>University of Alabama in Huntsville, 320 Sparkman Drive, Huntsville, AL 35805, USA

<sup>2</sup>Universities Space Research Association, 320 Sparkman Drive, Huntsville, AL 35805, USA

<sup>3</sup>Space Science Office, VP62, NASA/Marshall Space Flight Center, Huntsville, AL 35812, USA

<sup>4</sup>Max-Planck-Institut für extraterrestrische Physik (Giessenbachstrasse 1, 85748 Garching, Germany)

<sup>5</sup>School of Physics, University College Dublin, Belfield, Stillorgan Road, Dublin 4, Ireland

<sup>6</sup>Jacobs Technology

<sup>7</sup>Los Alamos National Laboratory, PO Box 1663, Los Alamos, NM 87545, USA

<sup>8</sup>Exzellenzcluster Universe, Technische Universität München, Boltzmannstrasse 2, 85748 Garching, Germany

to this series as more observations are accumulated by GBM.

Many correlative studies in the field of GRB global properties studies rely on only two very distinct representative spectra (Amati et al. 2002; Ghirlanda et al. 2004; Yonetoku et al. 2004). These are the *time-integrated* and *peak flux* spectra, representing (respectively) the average emission and the most luminous. Defining these uniformly is not trivial and trade-offs inevitably must be made. We have chosen to accumulate every spectrum that meets a minimum flux significance into our average spectrum, which leaves out quiescent periods that will dilute the signal. For the peak flux spectra we have chosen a slice of the burst representing the peak flux on a particular time scale. Because of the large dynamic range of burst durations (ms to thousands of s) we have chosen a smaller accumulation interval for those bursts with durations shorter than 2 s compared to those longer than 2 s. In this way, we can still make a distinction between the fluence and the peak flux spectra for the traditionally short-class GRBs.

The set of functions for fitting spectra was chosen for uniformity with the existing set of BATSE GRB Spectral Catalogs (Band et al. 1993; Kaneko et al. 2006; Goldstein et al. in prep.), as well as with the (forthcoming) GBM Time Resolved Spectroscopy Catalog of Bright Bursts. In most cases where the statistics of the spectra are sufficient, the data can support a number of free parameters that is rarely greater than four. Hence, we have selected spectral functions that simply exhibit two, three, and four free parameters. Our choice of the best model for each GRB, based upon the fit statistics, will be discussed below; however, for many cases it is clear when a simple model fails to fit the data, or when the fit does not significantly improve with a more complicated model.

We start with a brief description of the GBM detectors and calibration in Section 2 and refer to Meegan et al. (2009) and Bissaldi et al. (2009) for a more thorough and complete description of the instrument and calibration respectively. This is followed, in Section 3, by a description of the methodology used in the production of this catalog, including detector selection, data types used, energy selection and background fitting, and the source selection. We then offer a description of the spectral models used in this catalog in Section

4. In Section 5, we present the spectral analysis methods and results. A description of the Catalog file format can be found in the Appendix.

## 2. GBM Detectors and Calibration

GBM is one of two instruments on-board the *Fermi* Gamma-Ray Space Telescope, which was launched and placed into orbit on June 11, 2008. GBM is a 14-detector instrument designed to study the gamma-ray sky in the energy band of  $\sim 8$  keV–40 MeV. Twelve of the detectors are sodium iodide (NaI) scintillation detectors, placed in groups of three on the side edges of the spacecraft and pointed at various angles from the *Fermi* Large Area Telescope (LAT) boresight. The pointing angles were optimized through simulations to adequately survey the entire unocculted sky at any time during the orbit, while also biasing coverage toward the LAT pointing direction. The other two detectors are each composed of a bismuth germanate (BGO) crystal and are placed on either side of the spacecraft pointing at right angles to the LAT boresight. Each BGO crystal is coupled to two photomultiplier tubes, which collect the scintillation photons and convert them into electronic signals. The NaI detectors cover an energy range from 8 keV–1 MeV, and the BGO detectors cover a range of 200 keV–40 MeV. Because of the all-sky coverage of the NaI detectors, and the fact that the diameter of each NaI crystal (12.7 cm) is ten times its thickness, the approximate location of a burst can be determined by comparing the relative count rates in the detectors that observed the bursts. The source location is then calculated in spacecraft coordinates and used in the production of the detector response matrices (DRMs). The DRMs are mathematical models of the detectors' response used to map the observed counts into photons of known energy. Each detector's response is dependent on incident photon energy, the measured detector output energy, and the detector–source angle and the earth–source–spacecraft geometry.

A key issue for accurate spectroscopy is the fidelity of the detector calibration model, which matches detector pulse height analyzer (PHA) channels to physical energies. The individual GBM detectors were extensively calibrated before launch using several nuclear line sources

(Bissaldi et al. 2009). In addition to line sources, the BESSY accelerator in Berlin, Germany was used to determine the low-energy light output of four of the flight-qualified NaI detectors. Finally, a source survey calibration was performed on the entire assembled Fermi Observatory, just prior to observatory-level thermal vacuum testing. This last calibration consisted of several radioactive sources being individually placed at various angles relative to the observatory in order to verify and validate the spacecraft and instrument scattering models, used in the DRMs (Hoover et al. 2008).

Given that the lowest energy of the radioactive sources was 14.4 keV and that most of the detectors were not calibrated with a continuum energy source such as BESSY, it is useful to validate the GBM calibration using on-orbit observations of known astrophysical sources. A good spectroscopy standard is the Crab Nebula, which has been studied since the infancy of gamma-ray astronomy. However, GBM is not a pointed instrument, so we have made use of the Earth occultation technique, as pioneered with BATSE (Harmon et al. 2002). We have obtained excellent fits that are in good agreement in every detector with the canonical Crab Nebula spectrum (for details, see Case et al. 2011, Wilson-Hodge et al. in prep.). Notably, there are no systematic deviations in the residuals to the continuum fits that would indicate issues with the calibration. The Earth occultation technique uses 16 re-binned broad energy channels in the CSPEC data type (Meegan et al. 2009).

When some very bright sources have been fitted using the 128 energy channel CSPEC data type, a kink in the spectrum at  $\sim 33$  keV can be observed. This takes a ‘p-cygni’ type form, where some channels (at lower energies) lie below the fitted model and others (at higher energies) lie above it. The total extent in channel space is roughly 4–6 channels, while in energy space it is about 5–10 keV. Since the excess residuals have equal weight below and above the model fit and do not change the fitted parameters appreciably when the affected channels are excluded, we have chosen to ignore this effect in the current work. It is likely that the non-linear jump in the detector light output at the Na K-edge has not been modeled completely (see the NaI K-edge discussion in Bissaldi et al. (2009)), which we will address in future calibra-

tion work. As an example of non-linearity of the response, see Figure 1, which is the spectrum of the bright GRB 081009 using two NaI detectors.

Solar flares provide an additional means of calibration of the GBM detectors, particularly the high-energy BGO detectors. For example, the positron annihilation line (511 keV), neutron capture line (2.2 MeV), and various nuclear lines (e.g., 4.4 and 6.1 MeV) were observed with BGO detector 0 in the solar flare of 2010 June 12 (Abdo et al. in prep.), demonstrating the calibration of that detector. In that flare there was a small gain shift (1%), showing limitations of the gain adjustment software and the 511 keV line had an additional small offset (1%), possibly showing limitations of the energy calibration of the BGO detectors.

In addition to persistent, known sources, calibration of GBM can be studied with other transient events such as Soft Gamma Repeaters (SGRs). SGR bursts are short, with typical durations of several tens to a few hundred milliseconds. Their  $\nu F_\nu$  energy spectra typically peak around 40 keV with a very steep decline in flux above the peak. Analysis of all the SGR bursts detected by GBM is currently underway (see Lin et al. 2011; van der Horst et al., in preparation; von Kienlin et al., in preparation). Typically the models and fit parameters are consistent with those found from the observations of other instruments (for reviews, see Woods & Thompson (2006); Mereghetti (2008)). We fit the integrated count spectrum of one of the brightest bursts of SGR 1550 – 5418 observed by GBM. The spectrum is best fit with a model that agrees within the parameter uncertainties with the Israel et al. (2008) results obtained for SGR 1900+14 with *Swift*). This demonstrates the ability of the low-energy calibration to fit the overall spectrum well, except for the area around the NaI K-edge where we notice that the calibration is not adequate in removing instrumental effects, as discussed above.

Concerning the calibration of GBM with respect to GRBs, a number of efforts have been pursued to compare the GRB spectra attained by GBM to spectra obtained by other instruments observing the same bursts in approximately the same energy band. One of the first GRBs detected by GBM (GRB 080723B) was also observed by two instruments onboard the INTEGRAL space-

craft. A study (von Kienlin et al. 2009) was performed to compare GBM’s spectral analysis results with the ISGRI instrument (15 keV–1 MeV; Lebrun et al. 2003) and the SPI instrument (18 keV–8 MeV; Vedrenne et al. 2003). This burst was selected because it was bright, spectrally hard, and seen in most GBM detectors. This analysis was performed before the first in-flight calibration was released, and before an accurate modeling of the spacecraft solar panels, which could block or attenuate the observation from some detectors. A later study (Tierney et al. 2010) was performed on four other GRBs also detected by ISGRI, taking into account blocked detectors and a new in-flight calibration. These studies have confirmed that GRB spectra as measured by GBM are consistent with other well-established and calibrated instruments.

### 3. Method

During the first two years of operation, GBM triggered on 491 GRBs, 487 of which are presented in this catalog. The remaining bursts are excluded due to a low accumulation of counts or a lack of spectral/temporal coverage. In order to provide the most useful analysis to the community, we have attempted to make the method as systematic and uniform as possible. When we deviate from uniformity we indicate the circumstances clearly. Here we detail the detector and data selection as well as the process used to fit the data. Many of the criteria are adopted from the GBM Burst Catalog, (Paciesas et al., in prep.) and we have attempted to maintain this in all aspects. However, due to the nature of spectral analysis we demand stricter criteria to ensure that we have adequate signal in all energy channels. This also effectively reduces the GRB sample from that used in the burst catalog. In addition, this catalog includes 4 GRBs not included in the GBM Burst Catalog. GBM trigger number 081007.224 contains an observation of a GRB triggered by *Swift* (GRB 081007A; Baumgartner et al. 2009) at  $\sim 121$  s after GBM. The other three (GBM triggers 091013.989, 091022.752, & 091208.623) were originally classified as unknown triggers and were not included in the Burst Catalog, however their spectra are consistent with the GRB spectra observed by GBM. Two other triggers were classified as unknown, and the spectral analysis of those triggers reveal that

they are too weak to determine if they have GRB-like spectra.

#### 3.1. Detector Selection

GBM employs 14 detectors, situated at different angles to promote monitoring of the full unocculted sky: twelve NaI detectors with an energy coverage of 8 keV to 1 MeV and two BGO detectors with an energy coverage of 200 keV to 40 MeV. For this catalog, we use the data produced by both NaI and BGO detectors. GBM was designed to observe the entire unocculted sky at all times in order to increase the number of GRBs detected. However, when GBM triggers on a GRB, not all detectors have an optimal pointing for reconstructing the observed GRB spectrum. Therefore, we begin with all 12 NaI detectors and select a subset of these detectors with optimum viewing angles. To ensure sufficient detector response, we determined that using the detectors with viewing angles less than  $60^\circ$  from the location of a burst maximize the effective area and provide the best signal for spectral analysis, since the detector angle is strongly correlated with the count rate in the detector. In addition, we select the BGO detector that is closest to the NaI detectors in the subset. With this subset we run a program designed to determine any spacecraft blockage that would interfere with the signal. In most cases this provides a smaller subset of detectors that should be free of any blockage. However, due to small inaccuracies in the detector mass model or location uncertainties, the blockage code does not always return a subset of detectors that is free from blockage. This is evident when the low-energy data deviate strongly from the fit model, as depicted in Figure 2. This can affect particular detectors when the burst is partially occulted by the spacecraft. When this occurs we remove these detectors from the selected sample. Finally, in the event that more than 3 NaI detectors exist in our subsample for a particular burst, we discard all but the 3 detectors with the smallest source angles. This helps to prevent a fitting bias toward lower energies for bursts with more than 3 sufficient detectors, since the high significance of data in the NaI detectors will influence the spectral fitting procedure more than the lesser amount of data in the BGO detectors. With this final detector set for each burst, we have an adequate and reliable dataset for per-

forming spectral analysis.

### 3.2. Data Types

The primary data type used in this catalog was the time-tagged event (TTE) data, which provide absolute time resolution to  $2 \mu\text{s}$  based on GPS, and high energy resolution of 128 channels. For the purpose of this catalog, we choose a standard time binning of 1024 ms for bursts greater than 2 s in duration as defined by the burst  $t_{90}$  (see Paciesas et al. 2011) and 64 ms for bursts of duration 2 s and shorter. The time history of TTE typically starts at  $\sim 30$  s before trigger and extends to  $\sim 300$  s after trigger. This timespan is adequate for the analysis of most GRBs. For GRBs that have evident precursors or emissions that last more than 300 s after trigger, we use the CSPEC data, which extend  $\sim 4000$  s before and after the burst. This datatype also has a continuous 128 channel energy resolution which is normally accumulated at 4.096 s temporal resolution that changes to 1.024 s resolution for  $\sim 600$  s starting at trigger time. CSPEC data was used for 22 GRBs in this catalog.

### 3.3. Energy Selection and Background Fitting

With the optimum subset of detectors selected, the best time and energy selections are chosen to fit the data. The available reliable energy channels in the NaI detectors lie between  $\sim 8$  keV and  $\sim 1$  MeV. This selection excludes overflow channels and those channels where the instrument response is poor and the background is high. Since the issue with the sodium K-edge noticeably affects only the brightest GBM bursts, which comprise a small percentage of this catalog, we have chosen to keep the channels affected by the K-edge in the analysis of all GRBs. The fit parameters for bursts that are affected by non-linearity around the K-edge do not noticeably change; the only evident change in the results is the fit statistics and hence the goodness-of-fit. We perform a similar selection to the BGO detector for each burst, selecting channels between  $\sim 300$  keV and  $\sim 38$  MeV. With the resulting time series we select enough pre- and post-burst background to sufficiently model the background and fit a single energy dependent polynomial (choosing up to 4<sup>th</sup> order) to the background. For each detector the time selection and polynomial order are varied until the  $\chi^2$  statistic map over all energy

channels is minimized, resulting in an adequate background fit.

### 3.4. Source Selection

Once the background count rates are determined for each detector for a given burst, we sum the count rates and background models over all NaI detectors to produce a single lightcurve from which we make objective time selections. We subtract the background, convert the rates to counts, and calculate the signal-to-noise ratio (SNR) for each time history bin. Only the time bins that have a SNR greater or equal to 3.5 sigma are selected as signal. The time selections produced from this criterion are then applied to all detectors for a given burst. This criterion ensures that there is adequate signal to successfully perform a spectral fit and constrain the parameters of the fit. This does however eliminate some faint bursts from the catalog sample (i.e., those with no time bins with signal above 3.5 sigma). While this strict cut was performed to provide an objective catalog, it is possible that not all signal from a burst was selected. However, most of the signal below 3.5 sigma is likely indiscernible from the background fluctuations, so a spectral analysis including those bins would likely only increase the uncertainty in the measurements. This selection is what we refer to as the “fluence” selection, since it is a time-integrated selection, and the fluence derived is representative of the fluence over the total duration of the burst. The other selection performed is a 1.024 ms peak photon flux selection for long bursts and 64 ms peak count rate flux selection for short bursts as defined by their  $t_{90}$  duration (Paciesas et al. in prep.). This selection is made by adding the count rates in the NaI detectors again and selecting the single bin of signal with the highest background-subtracted count rate. This selection is a snapshot of the energetics at the most intense part of the burst. Figure 3 shows the distribution of accumulation time based on the signal-to-noise selection criteria. The accumulation time reported is similar to the observed emission time of the burst, excluding quiescent periods, (e.g. Mitrofanov et al. 1999). Figure 3 also includes the comparisons of the model photon fluence and photon flux compared to the accumulation time. Note that both comparisons contain two distinct regions associated with short

and long GRBs. While there appears to be a very clear correlation between the photon fluence and the accumulation time, there is little correlation between the burst-averaged photon flux and the accumulation time. However, the latter depicts a relationship similar to the hardness–duration relationship explored in Kouveliotou et al. (1993).

#### 4. Models

We chose four spectral models to fit the spectra of GRBs in our selection sample. These models include a single power law (PL), Band’s GRB function (BAND), an exponential cut-off power-law (COMP), and smoothly broken power law (SBPL). All models are formulated in units of photon flux with energy ( $E$ ) in keV and multiplied by a normalization constant  $A$  ( $\text{ph s}^{-1} \text{cm}^{-2} \text{keV}^{-1}$ ). Below we detail each model and its features.

##### 4.1. Power-Law Model

An obvious first model choice, ubiquitous in astrophysical spectra, is the single power law with two free parameters,

$$f_{PL}(E) = A \left( \frac{E}{E_{piv}} \right)^\lambda \quad (1)$$

where  $A$  is the amplitude and  $\lambda$  is the spectral index. The pivot energy ( $E_{piv}$ ) normalizes the model to the energy range under inspection and helps reduce cross-correlation of other parameters. In all cases in this catalog,  $E_{piv}$  is held fixed at 100 keV. While most GRBs exhibit a spectral break in the GBM passband, some weak GRBs are too weak to adequately constrain this break in the fits and therefore we chose to fit these with the PL model.

##### 4.2. Band’s GRB function

Band’s GRB function (Band et al. 1993) has become the standard for fitting GRB spectra, and therefore we include it in our analysis:

$$f_{BAND}(E) = A \begin{cases} \left( \frac{E}{100 \text{ keV}} \right)^\alpha \exp \left[ -\frac{(\alpha+2)E}{E_{peak}} \right], & E \geq \frac{(\alpha-\beta) E_{peak}}{\alpha+2} \\ \left( \frac{E}{100 \text{ keV}} \right)^\beta \exp(\beta - \alpha) \left[ \frac{(\alpha-\beta)E_{peak}}{100 \text{ keV} (\alpha+2)} \right]^{\alpha-\beta}, & E < \frac{(\alpha-\beta) E_{peak}}{\alpha+2} \end{cases}, \quad (2)$$

The four free parameters are the amplitude,  $A$ , the low and high energy spectral indices,  $\alpha$  and  $\beta$  respectively, and the  $\nu F_\nu$  peak energy,  $E_{peak}$ . This function is essentially a smoothly broken power law with a curvature defined by its spectral indices. The low-energy index spectrum is a power law only asymptotically.

##### 4.3. Comptonized Model

This model considered for GRB spectra is an exponentially cutoff power-law, which is a subset of the Band function in the limit that  $\beta \rightarrow -\infty$ :

$$f_{COMP}(E) = A \left( \frac{E}{E_{piv}} \right)^\alpha \exp \left[ -\frac{(\alpha+2) E}{E_{peak}} \right] \quad (3)$$

The three free parameters are the amplitude  $A$ , the low energy spectral index  $\alpha$  and  $E_{peak}$ .  $E_{piv}$  is again fixed to 100 keV, as is the case for the power law model. With the extended high-energy response of GBM compared to BATSE, we rarely suffer from an inability to measure the high-energy spectra of medium to strong intensity GRBs; however, we still find that the Comptonized model adequately describes many GRB spectra.

##### 4.4. Smoothly Broken Power-Law

The final model that we consider in this catalog is a broken power-law characterized by one break with flexible curvature able to fit spectra with both sharp and smooth transitions between the low and high energy power laws. This model, first published in Ryde (1999), where the logarithmic derivative of the photon flux is a continuous hyperbolic tangent, has been re-parametrized (Kaneko et al. 2006) as such:

$$f_{SBPL}(E) = A \left( \frac{E}{E_{piv}} \right)^b 10^{(a-a_{piv})} \quad (4)$$

where

$$\begin{aligned}
 a &= m\Delta \ln\left(\frac{e^q + e^{-q}}{2}\right), \\
 a_{piv} &= m\Delta \ln\left(\frac{e^{q_{piv}} + e^{-q_{piv}}}{2}\right), \\
 q &= \frac{\log(E/E_b)}{\Delta}, \quad q_{piv} = \frac{\log(E_{piv}/E)}{\Delta}, \\
 m &= \frac{\lambda_2 - \lambda_1}{2}, \quad b = \frac{\lambda_1 + \lambda_2}{2}.
 \end{aligned}
 \tag{5}$$

In the above relations, the low- and high-energy power law indices are  $\lambda_1$  and  $\lambda_2$  respectively,  $E_b$  is the break energy in keV, and  $\Delta$  is the break scale in decades of energy. The break scale is independent and not coupled to the power law indices as it is with the Band function, and as such represents an additional degree of freedom. However, Kaneko et al. (2006) found that an appropriate value for  $\Delta$  for GRB spectra is 0.3, therefore we fix  $\Delta$  at this value. Studies on the behavior of  $\Delta$  pertaining to GBM GRBs may be possible after more bright bursts have been detected; therefore this is left to possible future catalogs.

## 5. Data Analysis & Results

To study the spectra resulting from the GBM detectors, a method must be established to associate the energy deposited in the detectors to the energy of the detected photons. This association is dependent on effective area and the angle of the detector to the incoming photons. To do this, detector response matrices (DRMs) are used to convert the photon energies into detector channel energies. The DRM is a mathematical model of the deposition of photon energy in the crystal—a photon that interacts by the photoelectric effect will deposit 100% of its energy, subject to resolution broadening, while a photon that interacts by a single Compton scatter may deposit only a portion of its energy. The exception to this is when a photon carrying the energy of the iodine K-shell escapes the crystal. The energy calibration determines the energy boundaries of the energy deposition channels. The DRMs record this energy response of the detectors at various angles, which

was determined through extensive simulations using GRESS (Hoover et al. 2010) and validated by the source survey. The response matrices for all GRBs in the catalog were made using GBMRSP v1.9 of the response generator and version 2 of the GBM DRM database, and all responses employ atmospheric response modeling to correct for possible atmospheric interference. In particular, we use RSP2 files, which contain multiple DRMs based on the amount of slew the spacecraft experiences during the burst. A new DRM is calculated for every  $2^\circ$  of slew, changing the effective area of each detector based on its angle to the source. These DRMs are then all stored in a single RSP2 file for each detector. During the fitting process, each DRM is weighted by the counts fluence through the detector during each  $2^\circ$  slew segment.

The spectral analysis of all bursts was performed using RMfit, version 3.4rc1. RMfit employs a modified, forward-folding Levenberg-Marquardt algorithm for spectral fitting. The Castor C-Statistic, which is a modified log likelihood statistic based on the Cash parametrization (Cash 1979) is used in the model-fitting process as a figure of merit to be minimized. This statistic is preferable over the more traditional  $\chi^2$  statistic minimization because of the non-Gaussian counting statistics present when dividing the energy spectra of GBM GRBs into 128 channels. Although it is advantageous to perform the spectral fitting using C-Stat, this statistics provides no estimation of the goodness-of-fit, since there exists no standard probability distribution for likelihood statistics. For this reason, we also calculate  $\chi^2$  for each spectral fit that was performed through minimizing C-Stat. This allows an estimation of the goodness-of-fit of a function to the data even though  $\chi^2$  was not minimized. This also allows for easy comparison between nested models.

We fit the four functions described in Section 4 to the spectrum of each burst. The BAND and COMP functions are parametrized with  $E_{peak}$ , the peak in the power density spectrum, while the SBPL is parametrized with the break energy,  $E_{break}$ . We choose to fit these four different functions because the measurable spectrum of GRBs is dependent on intensity, as is shown in Figure 4. Observably less intense bursts provide less data to support a large number of parameters. This may appear obvious, but it allows us to deter-

mine why in many situations a particular empirical function provides a poor fit, while in other cases it provides an accurate fit. For example, the energy spectra of GRBs are normally well fit by two smoothly joined power laws. For particularly bright GRBs, the BAND and SBPL functions are typically an accurate description of the spectrum, while for weaker bursts the COMP function is most acceptable. Bursts that have signal significance on the order of the background fluctuations do not have a detectable distinctive break in their spectrum and so the power law is the most acceptable function. Although for weaker GRBs a model with more parameters is not statistically preferred, it is instructive to study the parameters of even the weaker bursts. In addition, the actual physical GRB processes can have an effect on the spectra and different empirical models may fit certain bursts better than others. The spectral results, including the best fit spectral parameters and the photon model, are stored in files following the FITS standard (see Appendix for file description) and are hosted as a public data archive on HEASARC<sup>1</sup>.

When inspecting the distribution of the parameters for the fitted models, we first define a data cut based on the goodness-of-fit. We require the  $\chi^2$  statistic for the fit to be within the  $3\sigma$  expected region for the  $\chi^2$  distribution of the given degrees of freedom, and we define a subset of each parameter distribution of this data cut as GOOD if the parameter error is within certain limits. Following Kaneko et al. (2006), for the low-energy power law indices, we consider GOOD values to have errors less than 0.4, and for high-energy power law indices we consider GOOD values to have errors less than 1.0. For all other parameters we consider a GOOD value to have a relative error of 0.4 or better. The motivation for this is to show well-constrained parameter values, rather than basing interpretations on parameters that are poorly constrained.

In addition, we define a BEST sample where we compare the goodness-of-fit of all spectral models for each burst and select the most preferred model based on the difference in  $\chi^2$  per degree of freedom. The criterion for accepting a model with a single additional parameter is a change in  $\chi^2$  of

at least 6 since the probability for achieving this difference is  $\sim 0.01$ . The parameter distributions are then populated with the spectral parameters from the BEST spectral fits.

### 5.1. Fluence Spectra

The time-integrated fluence spectral distributions admit results that are averaged over the duration of the observed emission. It should be noted that the following distributions do not take into account any spectral evolution that may exist within bursts. The low-energy indices, as shown in Figure 5, distribute about a  $-1$  power law typical of most GRBs. Up to 33% of the GOOD low-energy indices violate the  $-2/3$  synchrotron “line-of-death”, while an additional 62% of the indices violate the  $-3/2$  synchrotron cooling limit. The high-energy indices in Figure 6 peak at a slope slightly steeper than  $-2$  and have a long tail toward steeper indices. Note that the large number of unconstrained (or very steep) high-energy indices in the distribution of all high-energy index values indicates that a large number of GRBs are better fit by the COMP model, which is equivalent to a BAND function with a high-energy index of  $-\infty$ . The comparison of the simple power law index to the low- and high-energy indices makes evident that the simple power law index is averaged over the break energy, resulting in an index that is on average steeper than the low-energy index yet shallower than the high-energy index. We also show in Figure 6(d) the difference between the time-integrated low- and high-energy spectral indices,  $\Delta S = (\alpha - \beta)$ . This quantity is useful since the synchrotron shock model makes predictions of this value in a number of cases (Preece et al. 2002). The fluence spectra distribution of  $\Delta S$  bears resemblance to the time-resolved results in Preece et al. (2002), as well as time-integrated results in Kaneko et al. (2006).

In Figure 7, we show the distributions for the break energy,  $E_{break}$  and the peak of the power density spectrum,  $E_{peak}$ .  $E_{break}$  is the energy at which the low- and high-energy power laws are joined, which is not necessarily representative of the  $E_{peak}$ . The  $E_{break}$  for the SBPL has a strong clustering about 100 keV, while the peak for the BAND distribution is closer to 200 keV. The  $E_{peak}$  distributions all generally peak around 200 keV and cover just over two orders of mag-

<sup>1</sup><http://heasarc.gsfc.nasa.gov/W3Browse/fermi/fermigbrst.html>



nitude, which is consistent with previous findings (Mallozzi et al. 1995; Lloyd et al. 2000) from BATSE. As discussed in Kaneko et al. (2006), although the SBPL is parametrized with  $E_{break}$ , the  $E_{peak}$  can be derived from the functional form. We have calculated the  $E_{peak}$  for all bursts with low-energy index shallower than -2 and high-energy index steeper than -2, and we have used the covariance matrix to formally propagate and calculate the errors on the derived  $E_{peak}$ . The peak and overall distribution of  $E_{peak}$  is similar to that found by the BATSE Large Area Detectors, which had a much smaller bandwidth and larger collecting area. This would seem to indicate that it is unlikely for there to be a hidden population undiscovered by either instrument within the 20 keV - 2 MeV range. Additionally, the value of  $E_{peak}$  can strongly affect the measurement of the low-energy index of the spectrum, as shown in Figure 8. A general trend appears to show that lower  $E_{peak}$  values tend to increase the uncertainty in the measurement of the low-energy index, mostly due to the fact that a spectrum with a low  $E_{peak}$  will exhibit most of its curvature near the lower end of the instrument bandpass. In many cases, if the low-energy index is found to be reasonably steep ( $\lesssim -1$ ), the uncertainty of the index is minimized even if  $E_{peak}$  is low.

It is of interest to study the difference in the value of  $E_{peak}$  between the BAND and COMP functions since they are the two main functions used to study GRB spectra, and COMP is a special case of BAND. To study the relative deviation between the two values we calculate a statistic based on the difference between the values and taking into account their  $1\sigma$  errors. This statistic can be calculated by

$$\Delta E_{peak} = \frac{|E_{peak}^C - E_{peak}^B|}{\sigma_{E_{peak}}^C + \sigma_{E_{peak}}^B} \quad (6)$$

where C and B indicate the COMP and BAND values respectively. This statistic has a value of unity when the deviation between the  $E_{peak}$  values exactly matches the sum of the  $1\sigma$  errors. A value less than one indicates the  $E_{peak}$  values are within errors, and a value greater than one indicates that the  $E_{peak}$  values are not within errors of each other. Figure 9 depicts the distribution of the statistic and roughly 25% of the BAND and COMP  $E_{peak}$  values are found to be outside the

combined errors. This indicates that, although COMP is a special case of BAND, a significant fraction of the  $E_{peak}$  values can vary by more than  $1\sigma$  based on which model is chosen.

The distributions for the time-averaged photon flux and energy flux are shown in Figure 10. The photon flux peaks around 2 photons  $\text{cm}^{-2} \text{s}^{-1}$ , and the energy flux peaks at  $2.5 \times 10^{-7}$  ergs  $\text{cm}^{-2} \text{s}^{-1}$  in the 8-1000 keV band. When integrating over the full GBM spectral band, 8 keV - 40 MeV, the energy flux broadens and for all but the simple power law model, approximates a top hat function with a small high-flux tail spanning about 2 orders of magnitude. Note that the low-flux cutoff is due to the sensitivity of the instrument, and therefore the peak of the distributions are directly affected by the instrument sensitivity. A distribution of flux measurements with a more sensitive instrument will likely position the peak at a lower flux. Similarly in Figure 11, the distributions for the photon fluence and energy fluence are depicted. The plots for the photon fluence appear to contain evidence of the duration bimodality of GRBs, and have discriminant peaks at about 1 and 20 photons  $\text{cm}^{-2}$ . The energy fluence in the 8-1000 keV band peaks at about  $1 \times 10^{-6}$  erg  $\text{cm}^{-2}$ , while the peak in the 8 keV-40 MeV band shifts nearly an order of magnitude to about  $1 \times 10^{-5}$  erg  $\text{cm}^{-2}$  for all except the COMP model. The COMP model is largely unaffected by the change in energy band due to the exponential cutoff. The brightest GRB contained in this catalog based on time-averaged photon flux is GRB 081009 with a flux of  $> 30$  ph  $\text{s}^{-1} \text{cm}^{-2}$  and the burst with the largest average energy flux is GRB 090227B with an energy flux of  $\sim 1.3 \times 10^{-5}$  ergs  $\text{s}^{-1} \text{cm}^{-2}$ . The most fluent burst (although not the longest duration) in the catalog is GRB 090618 with a photon fluence of  $> 2600$  ph  $\text{cm}^{-2}$  and an energy fluence of  $> 2.5 \times 10^{-4}$  ergs  $\text{cm}^{-2}$ .

## 5.2. Peak Flux Spectra

The following peak flux spectral distributions have been produced by fitting the GRB spectra over the 1024 ms and 64 ms peak flux duration of long and short bursts respectively. Note that the results from both long and short bursts are included in the following figures. The low-energy indices from the peak flux selections, as shown in Figure 12, also distribute about the

typical  $-1$  power law. 42% of the GOOD low-energy indices violate the  $-2/3$  synchrotron “line-of-death”, while an additional 40% of the indices violate the  $-3/2$  synchrotron cooling limit, both of which are significantly larger percentages than those from the fluence spectra. The high-energy indices in Figure 13 peak at a slope slightly steeper than  $-2$  and again have a long tail toward steeper indices. The number of unconstrained high-energy indices increases when compared to the fluence spectra, likely due to the poorer statistics resulting from shorter integration times. As shown with the fluence spectra, the PL index serves as an average between low- and high-energy indices for the BAND and SBPL functions. Shown in Figure 13(d) is the  $\Delta S$  distribution for the peak flux spectra. This distribution is roughly consistent with the BATSE results found previously (Preece et al. 2002; Kaneko et al. 2006), but suffers from a deficit in values due in large part to the inability of the data to sufficiently constrain the high-energy power law index.

In Figure 14, we show the distributions for  $E_{break}$  and  $E_{peak}$ . As was evident from the fluence spectra, the  $E_{break}$  from the SBPL fits appears to peak at 100 keV, meanwhile the  $E_{break}$  from BAND is harder and peaks at about 200 keV. The  $E_{peak}$  distributions for all models peak around 150 keV and cover just over two orders of magnitude, which is consistent with previous findings (Preece et al. 1998; Kaneko et al. 2006). It should be noted that the data over the short timescales in the peak flux spectra do not often favor the SBPL model, resulting in large parameter errors. Using the propagation of errors scheme to calculate the  $E_{peak}$  for SBPL therefore causes many of the values to be largely unconstrained. This results in the much smaller  $E_{peak}$  distribution for SBPL seen in Figure 14(b). In addition, we calculate and show the  $\Delta E_{peak}$  statistic in Figure 15 and, as was the case with the fluence spectra,  $\sim 25\%$  of the BAND and COMP  $E_{peak}$  values are found to be outside the combined errors.

The distributions for the peak photon flux and energy flux are shown in Figure 16. The photon flux peaks around 4 photons  $\text{cm}^{-2} \text{s}^{-1}$ , and the energy flux peaks at  $7.4 \times 10^{-7}$  ergs  $\text{cm}^{-2} \text{s}^{-1}$  in the 8-1000 keV band. When integrating over the full GBM spectral band, 8 keV-40 MeV, the dispersion in the energy flux increases for all but

the simple power law model and approximates a top hat function with a small high-flux tail spanning about 2 orders of magnitude. The GRB with the brightest peak photon flux is GRB 081009 at  $> 130 \text{ ph s}^{-1} \text{ cm}^{-2}$ . This GRB is also the brightest GRB in terms of time-averaged photon flux which makes it an excellent burst for calibration studies. Similar to the time-averaged energy flux, the burst with highest peak energy flux is GRB 090227B at  $> 8.0 \times 10^{-5}$  ergs  $\text{s}^{-1} \text{ cm}^{-2}$ .

When studying the two types of spectra in this catalog, it is instructive to study the similarities and differences between the resulting parameters. Plotted in Figure 17 are the low-energy indices, high-energy indices, and  $E_{peak}$  energies of the peak flux spectra as a function of the corresponding parameters from the fluence spectra. Most of the peak flux spectral parameters correlate with the fluence spectral parameters on the order of unity. There are particular regions in each plot where outliers exist, and these areas are indications that either the GRB spectrum is poorly sampled or there exists significant spectral evolution in the fluence measurement of the spectrum that skews the fluence spectral values. Examples of the former case are when the low-energy index is atypically shallow ( $\gtrsim -0.5$ ) or the high-energy index is steeper than average ( $\lesssim -3$ ). An example where spectral evolution may skew the correlation between the two types of spectra is apparent in the comparison of  $E_{peak}$ . Here, it is likely that a fluence spectrum covering significant spectral evolution will produce a lower energy  $E_{peak}$  than is measured when inspecting the peak flux spectrum.

### 5.3. The BEST Sample

The BEST parameter sample produces the best estimate of the observed properties of GRBs. By using model comparison, the preferred model is selected, and the parameters are reviewed for that model. The models contained herein and in most GRB spectral analyses are empirical models, based only on the data received; therefore the data from different GRBs tend to support different models. Perhaps it will be possible to determine the physics of the emission process by investigating the tendencies of the data to support a particular model over others. It is this motivation, as well as the motivation to provide a sample that contains the best picture of the global properties

of the data, that prompts the investigation of the BEST sample.

In Table 1 we present the composition of models for the BEST samples. From this table, it is apparent that the fluence spectral data from GBM strongly favors the COMP model over the others in nearly half of all GRBs. The BAND and SBPL are favored by relatively few GRBs in the catalog. It should be noted that the number of GRBs best fit by PL increases in the peak flux spectra mainly due to the fact that the smaller statistics from the short integration time are unable to support a model more complex than the PL. In Figures 18 and 19 the same error cuts used in the GOOD samples were also used for the BEST parameters. Note that the PL index is statistically an averaging of the low- and high-energy power laws, and that, due to the fact that GBM spectral responses have a peak effective area at lower energies (below 100 keV), we have included PL indices in the BEST low-energy index distribution. Although in a number of cases the PL model is statistically preferred over the other models in this catalog, the spectral shape represented by the PL is inherently different from the shape of the other models. Therefore, the PL index is not necessarily representative of either the low- or high-energy indices from the other models. In Figures 18(a) and 19(a) we show where the distribution of PL indices exists relative to the alpha and beta distributions. The PL index represents 25% of the BEST fluence alpha distribution and 50% of the BEST peak flux alpha distribution. The fluence spectra, on the whole, have a steeper measured alpha and shallower beta than the peak flux spectra. The alpha distribution for the fluence spectra peaks at about  $-1$ , while the peak flux low-energy spectral index peaks at about  $-0.6$ . Conversely, the beta distribution for the fluence spectra peaks at  $-2.1$  and the peak flux high-energy spectral index peaks at  $-2.4$ . As shown before for the GOOD spectra, Figure 20 shows the  $\Delta S$  distributions for the BEST fluence and peak flux spectra. Both distributions are found to be consistent with previous investigations into BATSE time-integrated and time-resolved spectra (Preece et al. 2002; Kaneko et al. 2006)

Additionally, the  $E_{peak}$  (Figure 18(b)) and  $E_{break}$  (19(b)) distributions differ between the two spectra. The fluence spectra  $E_{peak}$  peaks

near 200 keV and the  $E_{break}$  peaks at about 150 keV, although the kurtosis of the distribution is much lower than that of the  $E_{peak}$  distribution. Meanwhile, the  $E_{peak}$  and  $E_{break}$  for the peak flux spectra both peak at about 150 keV. As is shown in Figures 18(c) and 19(c) the photon flux does not significantly change when widening the energy band from 8 keV–1 MeV to 8 keV–40 MeV. The fluence spectra photon flux peaks around 1.5 photons  $\text{cm}^{-2} \text{s}^{-1}$  and the peak flux photon flux peaks around 4 photons  $\text{cm}^{-2} \text{s}^{-1}$ . Alternatively, the energy flux is greatly affected by expanding the energy band, as is shown in Figures 18(d) and 19(d). Specifically, the distribution in the 8 keV–1 MeV band peak around a few  $\times 10^{-7}$  ergs  $\text{cm}^{-2} \text{s}^{-1}$ , but in the 8 keV–40 MeV band the distribution broadens significantly and becomes much less peaked, approaching what appears to be a top hat distribution.

To aid in the study of the systematics of the parameter estimation, as well as the garner the effect statistics has on the fitting process, we investigate the behavior parameter values as a function of the photon fluence and peak photon flux for the fluence and peak flux BEST spectra respectively. These distributions are shown in Figures 21 and 22. When fitting the time-integrated spectrum of a burst, we find the low- and high-energy indices trend toward steeper values for exceedingly more fluent spectra. The simple PL index trends from shallow value of  $\sim -1.3$  to a steeper value of  $\sim -2$ . The low-energy index for a spectrum with curvature tends to exhibit an unusually shallow value of  $\sim -0.4$  for extremely low fluence spectra, and steepens to  $\sim -1.5$ . Similarly, the high-energy index trends from  $\sim -1.6$  at low fluence to  $\sim -2.7$  at high fluence, although this is complicated by unusually steep and poorly constrained indices that indicate that an exponential cutoff may result in a more reliable spectral fit. When inspecting the  $E_{peak}$  as a function of photon fluence, a trend is much less apparent. If a burst is assumed to have significant spectral evolution, then obviously the  $E_{peak}$  will change values through the time history of the burst, typically following the traditional hard-to-soft energy evolution. For this reason, spectra that integrate over increasingly more time will tend to suppress the highest energy of  $E_{peak}$  within the burst, so a general decrease in  $E_{peak}$  is expected with longer integration times. However,

the photon fluence convolves the integration time with the photon flux so that an intense burst with a short duration may have on the order the same fluence as a much longer but less intense burst but results in a higher  $E_{peak}$ . This causes significant broadening to the decreasing trend as shown in Figure 21(c). The distribution of parameters as a function of the peak photon flux, however, is much less clear. The distributions shown in Figure 22 are more susceptible to uncertainty because of the generally smaller statistics involved in study the peak flux section of the GRB, except in some cases where the peak photon flux is on the order of the photon fluence. Ignoring the regions where the parameters are poorly constrained, another trend emerges from the low-energy indices; they appear to become slightly more shallow as the photon flux increases. The high-energy indices, however, appear to be unaffected by the photon flux, except those that are unusually steep and indicate that an exponential cutoff may be preferred. Finally, no obvious trend is visible for  $E_{peak}$  as a function of the peak photon flux. This likely results from the fact that neither spectral index in the peak flux spectrum is affected much by the photon flux.

#### 5.4. $\chi^2$ Distributions

Although the least-squares fitting process did not minimize  $\chi^2$  as a figure of merit, we can calculate the  $\chi^2$  goodness-of-fit statistic comparing the model to the data. To do this, we difference the background-subtracted count rates from the model rates, summing first over all energy channels in each detector, and then over all detectors. This is shown by

$$\chi^2 = \sum_i \sum_j \left[ \frac{O_{ij} - B_{ij} - M_{ij}}{\sqrt{\sigma_{M_{ij}}^2}} \right]^2, \quad (7)$$

where the  $O_{ij}$  are the observed count rates,  $B_{ij}$  are the background rates,  $M_{ij}$  are the model rates, and  $\sigma_{M_{ij}}^2$  are the derived model variances. In the ideal situation and assuming acceptable spectral fits (i.e. when performing spectral analysis of simulated data), the reduced  $\chi^2$  value ( $\chi^2/\text{d.o.f.}$ ) will tend to distribute around a value of 1. In this way,  $\chi^2$  gives an estimate on the acceptability of the fit. Figure 23 shows the reduced  $\chi^2$  distributions for both the fluence and peak flux spectra, as well as

the corresponding BEST distributions. It is important to note that the distributions all peak at slightly larger values than 1, which is acceptable since the fits did not minimize  $\chi^2$  and even the BEST spectral fits represent an approximation to the actual spectra of GRBs due to their empirical nature. The fluence  $\chi^2$  distributions appear to be much broader and shifted farther from the nominal reduced  $\chi^2$  value than the peak flux distributions. This is likely due to the longer time integration intervals in the fluence spectra and the fact that many GRBs experience spectral evolution. The peak flux sample captures the spectra of all bursts in a small slice of time at the same stage of the lightcurve, meanwhile the fluence sample integrates over the duration of the emission, in many cases over several pulses. The proximity of most of the reduced  $\chi^2$  values to the nominal value is indicative of acceptable spectral fits.

In addition, Figure 24 plots the BEST reduced  $\chi^2$  as a function of photon fluence and peak photon flux for the fluence and peak flux spectra respectively. The reduced  $\chi^2$  for the fluence fits shows a marked upward trend as the photon fluence increases. The average reduced  $\chi^2$  starts at approximately a value of unity at a low fluence of  $\sim 0.2$  photons  $\text{cm}^{-2}$  and increases to a value of  $\sim 2$  at  $\sim 1000$  photons  $\text{cm}^{-2}$ . Additionally there are several outliers to the trend that exist at high fluence and exhibit even larger reduced  $\chi^2$  values. This indicates that the goodness-of-fit is increasingly worse the more fluent the burst. This follows from the fact that in most cases extremely fluent bursts are long and may exhibit significant spectral evolution, therefore the time-integrated spectral fit will average over the evolution and will produce a significantly worse fit. When inspecting the reduced  $\chi^2$  as a function of the photon flux, we find that the trend is not as dramatic, with low flux spectra producing a marginally better goodness-of-fit than the high flux spectra. This indicates that the peak flux spectra do not suffer from the same systematic effects as the fluence spectra. Most of the large reduced  $\chi^2$  values from the peak flux spectra result from high flux bursts where the problem around the K-edge dominates the statistics of the goodness-of-fit.

## 6. Summary & Discussion

GBM has allowed the observation of a large number of GRB spectra over a broad energy range that has not been fully covered previously. The broad energy range of GBM translates to parameter distributions that are variants of distributions found by previous instruments (e.g. Kaneko et al. 2006, Goldstein et al. in prep. on the final BATSE spectral catalog). The distributions contained here are similar to those shown by previous studies, yet contain differences that display the usefulness of studying GRBs over different energy bands and sensitivities. Although the typical average GRB spectrum has largely remained unchanged within the GBM energy band, the distributions of spectral parameters are no longer as narrow as previously thought. We have shown in many cases that the fitted spectrum of a GRB depends in large part on its intensity as well as the detector sensitivity. This observation implies that weak GRBs may have the same inherent spectrum as their more intense counterparts, yet we are unable to accurately determine their spectrum, reinforcing the importance of comparing the spectral parameter distributions from different acceptable models. Additionally, the high-energy coverage provided by the BGO detectors allows the extension of fine spectral analysis into a new regime. For example, the inclusion of high-energy data in many cases causes the high-energy power law to soften, and in some cases provides evidence for spectral cutoffs at even higher energies that is being investigated by the *Fermi*/LAT (Omodei et al. in prep.). Because of the high-energy coverage, we have uncovered several GRBs with peak energies greater than 1 MeV, extending the  $E_{peak}$  distribution to higher energies. Observations of high-  $E_{peak}$  GRBs have been observed previously (e.g. GRB 990123; Briggs et al. 1999), but were typically not from time-integrated spectra. According to our BEST samples, 18 GRBs have a time-integrated  $E_{peak}$  larger than 1 MeV, which is  $\sim 6\%$  of the GRB fluence spectra in the catalog that can be fitted with a curved function. Similarly, 8 GRBs have a peak flux  $E_{peak}$  greater than 1 MeV, which is  $\sim 5\%$  of the peak flux spectra that can be fit by a curved function (for details on three short hard bursts see Guiriec et al. 2010).

Another interesting result of the parameter dis-

tributions is the  $\Delta S$  parameter, the difference between the low- and high-energy spectral indices. This can be an important quantity because current models for the GRB prompt emission mechanism can be broken into two categories: magnetic (e.g. Lee et al. 2000) or internal/external shock (e.g. Rees & Meszaros 1992) driven. Implications about the shock driven case can be drawn directly from  $\Delta S$ . Sari et al. (1998) presented a model for the prompt emission spectrum where the emission of synchrotron photons by shock accelerated electrons evolves due to radiative and adiabatic losses. A key prediction of this model is a series of relationships between the photon spectral indices above and below the synchrotron peak. Preece et al. (2002) found that this relationship can be used to constrain the synchrotron cooling regime of the electrons by looking at the difference of the Band function spectral indices across the  $\nu F_\nu$  peak. Therefore, investigating  $\Delta S$  potentially provides insight into the emission mechanism of GRBs by comparing  $\Delta S$  to the prediction offered by the synchrotron shock model.

A comparison between different catalogs can be instructive, especially when noting the difference in methodologies and analysis. For example, the methodology and fit results for GBM bursts presented in Nava et al. (2011) are somewhat different than the analysis and results given in this GBM catalog. Simple differences in data selection and methodology, such as analysis on detectors with spacecraft blockage and usage of detectors with detector-to-source angles larger than  $60^\circ$ , can significantly affect the results of the spectral analysis. Additionally, in the Nava et al. (2011) sample, signal selections were not performed in a systematic way, but rather subjectively selected, based on a subjective estimate of where the signal fell below the background. These differences as well as many others can lead to large differences in results. We have compared the overall average values and distributions between this catalog and the analysis of Nava et al. (2011). Nava et al. (2011) report which model is most preferred for each burst in their sample; however they do this by comparing C-Stat, which does not allow for model comparison without Monte Carlo simulation for each burst. Unfortunately, a  $\chi^2$  goodness-of-fit is also not reported so there is no clue to the accuracy of their model selection method, nor

how well their models actually fit the data. This should also be noted as a caveat when comparing the two catalogs. Table 3 shows the sample mean and standard deviation of Nava et al. (2011) and a comparison to the results of this catalog, of which there are many notable differences. Although their average best low-energy index value for the time-integrated spectra is relatively similar, their average high-energy index is found to be steeper and represents a narrower distribution, although this may be due to their stated inability to constrain the high-energy index. Their average  $E_{peak}$  value is slightly softer and does not capture as many of the extended high-energy  $E_{peak}$  values that are found in this catalog. The mean time-averaged energy flux is also softer by about 25% compared to our derived values. The differences in the peak flux spectra are even more divergent. The average low-energy index found by Nava et al. (2011) is surprisingly shallow and the high-energy index is somewhat steeper and represents a much broader distribution than what is presented here. They found the average  $E_{peak}$  of the peak flux spectra to be somewhat harder, but their average peak energy flux is nearly an order of magnitude larger than reported in this catalog. These differences are representative of divergent methodologies and samples; therefore the reader should take care to understand how the values in the catalogs are derived.

Additionally, when comparing our results to the BATSE catalog of bright GRBs (Kaneko et al. 2006), there are some marked differences as well, although many of these arise because the Kaneko et al. (2006) sample studied only the 350 brightest BATSE GRBs. We investigated the sample mean of the time-integrated spectra for comparison (see Table 3) and found that the average low-energy index was relatively the same and the high-energy index on average was slightly steeper. The difference of values in the high-energy index could perhaps be explained by the difference in spectral bandwidth between the two instruments. The time-averaged  $E_{peak}$  however, is on average harder, most likely due to the selection of the brightest bursts in that catalog. This also affects the  $E_{break}$ , which is considerably harder at over 200 keV, and naturally the Kaneko et al. (2006) catalog reports larger average photon and energy fluxes and much larger spreads in flux due to the

increased sensitivity compared to GBM.

In conclusion, we have presented a systematic analysis of GRBs detected by GBM during its first two years of operation. This catalog contains four basic photon model fits to each burst, using two different selection criteria to facilitate an accurate estimate of the spectral properties of these GRBs. We have described subsets of the full results in the form of data cuts based on parameter uncertainty, as well as employing model comparison techniques to select the most statistically preferred model for each GRB. The analysis of each GRB was performed as objectively as possible, in an attempt to minimize biased systematic errors inherent in subjective analysis. The methods we have described treat all bursts equally, and we have presented the ensemble observed spectral properties of GBM GRBs. Certainly there are avenues of investigation that require more detailed work and analysis or perhaps a different methodology. This catalog should be treated as a starting point for future research on interesting bursts and ideas. As has been the case in previous GRB spectral catalogs, we hope this catalog will be of great assistance and importance to the search for the physical properties of GRBs and other related studies.

## 7. Acknowledgments

AG acknowledges the support of the Graduate Student Researchers Program funded by NASA. SMB acknowledges support of the European Union Marie Curie Reintegration Grant within the 7th Program under contract number PERG04-GA-2008-239176. SF acknowledges the support of the Irish Research Council for Science, Engineering, and Technology, co-funded by Marie Curie Actions under FP7. The GBM project is supported by the German Bundesministeriums für Wirtschaft und Technologie (BMWi) via the Deutsches Zentrum für Luft und Raumfahrt (DLR) under the contract numbers 50 QV 0301 and 50 OG 0502

## A. Spectral Catalog Data Files (SCATs)

The spectral fit results are stored in a series of Flexible Image Transport System (FITS) data files, available online from NASA's High Energy Astrophysics Science Archive Research Center (HEASARC)<sup>2</sup>. This data product provides different types of spectral fits to be included in the official spectral catalog of GBM bursts. The type is coded into the filename. There are two types of spectrum categories:

1. Peak flux ('pflx') - a single spectrum over the time range of the burst's peak flux
2. Fluence ('flnc') - a single spectrum over the entire burst

The time ranges for each category are included with the spectra. The spectra are fit with a number of models, whose complexity often depends on the signal-to-noise ratio of the spectrum. The current set is:

1. Power law ('plaw'),
2. Comptonized (exponentially attenuated power law; 'comp')
3. Band ('band')
4. Smoothly broken Power Law ('sbpl')

The set of detectors used for the fit is not coded into the filename, and may not be the same as the set of detectors that triggered. The file naming convention is thus: `glg_scat_all_bnymmddfff_type_mod1_vxx.fit`, with `yymmdd` = the date; `fff` = fraction of a day, in thousandths; `xx` = version number of the file; `type` = 'pflx' or 'flnc', the spectral categories; and `mod1` = 'plaw', 'comp', 'band', or 'sbpl', the spectral model used. We have chosen to designate burst triggers by the fraction of a day in thousandths, because that time (86.4 s.) is less than the time for a complete trigger data readout, as currently defined in the GBM Flight Software (300 s.). Therefore, we will not confuse two successive triggers by name.

FITS files are generally self-documenting, consisting of header and data pairs, where the ASCII headers are human readable and are followed by the data, as described in the header format statements, in either ASCII or binary format. The first (or, 'primary') header describes the file's content in general, and includes information that applies globally. The data section for the primary header is an optional image, and the GBM data files omit this. An example primary header is as follows:

```
SIMPLE =                               T /Written by IDL:  Mon Feb 14 13:36:27 2011
BITPIX =                               8 /
NAXIS  =                               0 /
EXTEND  =                               T /File contains extensions
DATE   = '2011-02-14T19:36:28' /
FILETYPE= 'SPECTRAL FITS'              /Unique FITS file type name
CREATOR = 'rmfit 3.4rc1'                /Software/version creating file
ORIGIN  = 'GIOC'                        /Name of organization
TELESCOP= 'GLAST'                       /Name of mission
INSTRUME= 'GBM'                         /Name of instrument
OBSERVER= 'Meegan'                      /Name of instrument PI
MJDREFI =                               51910.0 /MJD date of reference epoch, int part
MJDREFF = 7.428703703703703E-04 /MJD date of reference epoch, frac part
TIMESYS = 'TT'                          /Time system
TIMEUNIT= 's'                           /Time unit used in TSTART, TSTOP and TRIGTIME
OBJECT  = 'GRB081101167'                /
```

<sup>2</sup><http://heasarc.gsfc.nasa.gov/W3Browse/fermi/fermigbrst.html>

```

DATE-OBS= '2008-11-01T04:00:38' /Date of start of observation
DATE-END= '2008-11-01T04:00:39' /Date of start of observation
TSTART   =    247204838.5854399 /Observation start time, relative to MJDREF
TSTOP    =    247204839.6094399 /Observation end time, relative to MJDREF
TRIGTIME=    247204840.6334400 /Trigger time, relative to MJDREF
FILENAME= 'glg_scat_all_bn081101167_flnc_band_v02.fit' /Name of FITS file
COMMENT This file consists of time-sequenced spectral fit parameters
CHECKSUM= 'ZTAQbT4QZTAQbT3Q' / HDU checksum updated 2011-02-14T19:36:28
DATASUM  = '      0' / data unit checksum updated 2011-02-14T19:36:28
END

```

Here, we find that the event named 'GRB081101167' (OBJECT), triggered at 247204840.6334400 s Fermi Mission Elapsed Time (TRIGTIME), or roughly 4 hours, 0 minutes and 38 seconds on November 1, 2008 UTC. In addition to this, the standard header information gives the name of the file itself, the creation time and program version, as well as where the file originated and details of the mission and instrument with which it is associated. Finally, EXTEND is true, so the primary header is followed by one or more extensions. One cannot assume that the order of these extensions will be preserved, however they have identifiers that will allow readers to access the correct one. The original GBM files will always follow the order as given here.

The first data extension describes the detectors used and the selections made, both in time and energy (channel), for the spectral fit. The unique name (EXTNAME) for this extension and its structure is 'DETECTOR DATA':

```

XTENSION= 'BINTABLE' /Written by IDL: Mon Feb 14 13:36:27 2011
BITPIX = 8 /
NAXIS = 2 /Binary table
NAXIS1 = 244 /Number of bytes per row
NAXIS2 = 3 /Number of rows
PCOUNT = 6156 /Random parameter count
GCOUNT = 1 /Group count
TFIELDS = 12 /Number of columns
TFORM1 = '20A' /Character string
TTYPER1 = 'INSTRMNT' /Instrument name for this detector
TFORM2 = '20A' /Character string
TTYPER2 = 'DETNAM' /Detector number; if one of several available
TFORM3 = '20A' /Character string
TTYPER3 = 'DATATYPE' /Data type used for this analysis
TFORM4 = '20A' /Character string
TTYPER4 = 'DETSTAT' /Was this detector INCLUDED or OMITTED
TFORM5 = '60A' /Character string
TTYPER5 = 'DATAFILE' /File name for this dataset
TFORM6 = '60A' /Character string
TTYPER6 = 'RSPFILE' /Response file name for this dataset
TFORM7 = '60A' /Character string
TTYPER7 = 'FIT_INT' /Fit intervals
TFORM8 = '1J' /Integer*4 (long integer)
TTYPER8 = 'CHANNUM' /Total number of energy channels for this detecto
TFORM9 = '2J' /Integer*4 (long integer)
TTYPER9 = 'FITCHAN' /Channels selected in fitting this detector
TFORM10 = '1PE(129)' / Real*4 (floating point), variable length
TUNIT10 = 'keV' /
TTYPER10 = 'E_EDGES' /Energy edges for each selected detector

```



```

TFORM11 = '1PE(128)'           / Real*4 (floating point), variable length
TUNIT11 = 'Photon cm^-2 s^-1 keV^-1' /
TTYPER11 = 'PHTCNTS '         /Array of photon counts data
TFORM12 = '1PE(128)'           / Real*4 (floating point), variable length
TUNIT12 = 'Photon cm^-2 s^-1 keV^-1' /
TTYPER12 = 'PHTMODL '         /Array of photon model data
TFORM13 = '1PE(128)'           / Real*4 (floating point), variable length
TUNIT13 = 'Photon cm^-2 s^-1 keV^-1' /
TTYPER13 = 'PHTERRS '         /Array of errors in photon counts data
DATE     = '2011-02-14T19:36:28' /
EXTNAME  = 'DETECTOR DATA'     /Name of this binary table extension
ORIGIN   = 'GIOC '              /Name of organization
TELESCOP= 'GLAST '             /Name of mission
INSTRUME= 'GBM '               /Name of instrument
OBSERVER= 'Meegan '           /Name of instrument PI
MJDREFI  = 51910.0 /MJD date of reference epoch, int part
MJDREFF  = 7.428703703703703E-04 /MJD date of reference epoch, frac part
TIMESYS  = 'TT '              /Time system
TIMEUNIT= 's '                /Time unit used in TSTART, TSTOP and TRIGTIME
DATE-OBS= '2008-11-01T04:00:38' /Date of start of observation
DATE-END= '2008-11-01T04:00:39' /Date of start of observation
TSTART   = 247204838.5854399 /Observation start time, relative to MJDREF
TSTOP    = 247204839.6094399 /Observation end time, relative to MJDREF
TRIGTIME= 247204840.6334400 /Trigger time (s) relative to MJDREF
NUMFITS  = 1 /Number of spectral fits in the data
CHECKSUM= 'H7PaJ5NYH5NaH5NW' / HDU checksum updated 2011-02-14T19:36:28
DATASUM  = '1048916985'       / data unit checksum updated 2011-02-14T19:36:28
END

```

Since NAXIS2 is 3, three detectors were used for this fit; the data must be read in the DETECTOR column to determine which ones. Descriptive ASCII text data identifies which of the GBM detectors were chosen (DETECTOR; e.g. 'BGO\_00'), which data type was selected (DATATYPE; e.g. 'TTE'), the original GBM data file name (DATAFILE; e.g. 'glg\_tte\_b0\_bn081101167\_v01.fit'), and the time and energy selection intervals (FIT\_INT; e.g. '-2.048: -1.024 s, 284.65: 37989. keV, channels 3: 123'). Detector-specific binary data consist of the PHA channel energy edges (E\_EDGES), the deconvolved 'photon' counts (PHTCNTS) and uncertainties (PHTERRS), used to reconstruct a plot of the deconvolved fit in photon space, rather than counts space, where the observed data were actually fitted, using the counts model (PHTMODL). The number of energy edges is one more than the number of PHA channels, since they represent bin boundaries; or, physically, they are the energy loss thresholds in the detector, along with one more edge to complete the last bin.

Finally, there is an extension (EXTNAME = 'FIT PARAMS') that describes the spectral fit in detail:

```

XTENSION= 'BINTABLE'           /Written by IDL: Mon Feb 14 13:36:27 2011
BITPIX   = 8 /
NAXIS    = 2 /Binary table
NAXIS1   = 110 /Number of bytes per row
NAXIS2   = 1 /Number of rows
PCOUNT   = 96 /Random parameter count
GCOUNT   = 1 /Group count
TFIELDS  = 15 /Number of columns
TFORM1   = '2D '              /Real*8 (double precision)
TTYPER1  = 'TIMEBIN '         /Start and stop times relative to trigger

```

```

TFORM2 = '3E      ' /Real*4 (floating point)
TTYPE2 = 'PARAM0 ' /Band's GRB, Epeak: Amplitude
ASYMERO =          0 /Corresponding PARAM contains (value, +/- error)
TFORM3 = '3E      ' /Real*4 (floating point)
TTYPE3 = 'PARAM1 ' /Band's GRB, Epeak: Epeak
ASYMER1 =          0 /Corresponding PARAM contains (value, +/- error)
TFORM4 = '3E      ' /Real*4 (floating point)
TTYPE4 = 'PARAM2 ' /Band's GRB, Epeak: alpha
ASYMER2 =          0 /Corresponding PARAM contains (value, +/- error)
TFORM5 = '3E      ' /Real*4 (floating point)
TTYPE5 = 'PARAM3 ' /Band's GRB, Epeak: beta
ASYMER3 =          0 /Corresponding PARAM contains (value, +/- error)
TFORM6 = '2E      ' /Real*4 (floating point)
TTYPE6 = 'PHTFLUX ' /Photon Flux (ph/s-cm^2) std energy (8-1000)
TFORM7 = '2E      ' /Real*4 (floating point)
TTYPE7 = 'PHTFLNC ' /Photon Fluence (ph/cm^2) std energy (8-1000)
TFORM8 = '2E      ' /Real*4 (floating point)
TTYPE8 = 'NRGFLUX ' /Energy Flux (erg/s-cm^2) std energy (8-1000)
TFORM9 = '2E      ' /Real*4 (floating point)
TTYPE9 = 'NRGFLNC ' /Energy Fluence (erg/cm^2) std energy (8-1000)
TFORM10 = '2E     ' /Real*4 (floating point)
TTYPE10 = 'REDCHSQ ' /Reduced Chi^2 (1) and fitting statistic (2)
TFORM11 = '1I     ' /Integer*2 (short integer)
TTYPE11 = 'CHSQDOF ' /Degrees of Freedom
TFORM12 = '2E     ' /Real*4 (floating point)
TTYPE12 = 'PHTFLUXB' /Photon Flux (ph/s-cm^2) BATSE energy (50-300)
TFORM13 = '2E     ' /Real*4 (floating point)
TTYPE13 = 'DURFLNC ' /Photon Fluence (ph-cm^2) for durations (user)
TFORM14 = '2E     ' /Real*4 (floating point)
TTYPE14 = 'NRGFLNCB' /Energy Fluence (erg-cm^2) BATSE energy (50-300)
TFORM15 = '16E    ' /Real*4 (floating point)
TTYPE15 = 'COVARMAT' /Covariance matrix for the fit (#free params ^2)
TDIM15 = '(4, 4) ' /COVARMAT array dimensions
DATE    = '2011-02-14T19:36:28' /
ORIGIN  = 'GIOC   ' /Name of organization
TELESCOP= 'GLAST  ' /Name of mission
INSTRUME= 'GBM    ' /Name of instrument
OBSERVER= 'Meegan ' /Name of instrument PI
MJDREFI =          51910.0 /MJD date of reference epoch, int part
MJDREFF = 7.428703703703703E-04 /MJD date of reference epoch, frac part
TIMESYS = 'TT     ' /Time system
TIMEUNIT= 's      ' /Time unit used in TSTART, TSTOP and TRIGTIME
OBJECT  = 'GRB081101167' /
DATE-OBS= '2008-11-01T04:00:38' /Date of start of observation
DATE-END= '2008-11-01T04:00:39' /Date of start of observation
TSTART  = 247204838.5854399 /Observation start time, relative to MJDREF
TSTOP   = 247204839.6094399 /Observation end time, relative to MJDREF
TRIGTIME= 247204840.6334400 /Trigger time (s) relative to MJDREF
NUMFITS =          1 /Number of spectral fits in the data
N_PARAM =          4 /Total number of fit parameters (PARAMn)

```

```

FLU_LOW =          10.0000 /Lower limit of flux/fluence integration (keV)
FLU_HIGH=          1000.00 /Upper limit of flux/fluence integration (keV)
STATISTIC= 'Castor C-STAT' /Indicates merit function used for fitting
EXTNAME = 'FIT PARAMS' /Name of this binary table extension
CHECKSUM= 'Vc2jVc2hVc2hVc2h' / HDU checksum updated 2011-02-14T19:36:28
DATASUM = '3846818573' / data unit checksum updated 2011-02-14T19:36:28
END

```

The start and end times of the spectral accumulation are found in the 'TIMEBIN' array. This and the following columns are designed for several spectra results to be stored in a single file, as would be the case for time-resolved spectroscopy; for the purposes of the present work, there are only the results for a single fit. The following set of columns, labeled with 'PARAMn', where 'n' is an integer, contain both a fit parameter and the associated uncertainty. The comment for the column contains the name of the function fitted as well as the parameter name, separated by a colon. So, for instance, the data column 'PARAM1' contains the fitted Band GRB function  $E_{\text{peak}}$  parameter and uncertainty. If the corresponding 'ASYMERn' keyword is 0 then the 'PARAMn' columns contain symmetric errors, and if the keyword is 1 then the 'PARAMn' columns contain the asymmetric errors. All files created for this catalog contain symmetric errors only.

The last parameter column ('PARAMn') is followed by nine standard analysis products, in turn followed by the covariance matrix for the fit. The analysis products are fluxes and fluence values, calculated over several different energy ranges, calculated by integrating the fitted photon model at high energy resolution. For the columns labelled, 'PHTFLUX', 'PHTFLNC', 'NRGFLUX' and 'NRGFLNC', the standard energy range for integration is given in the 'FLU\_LOW' and 'FLU\_HIGH' keyword values; in this case, 10 to 1000 keV. The columns with names beginning with 'NRG' indicate that the corresponding value has been multiplied by the photon energy before integrating. The uncertainties associated with these values have been determined by numerically evaluating the partial derivative with respect to each free parameter in the fit and multiplying these into the covariance matrix (found in the column 'COVARMAT', as a flattened row vector with  $n \times n$  elements,  $n$  being the total number of parameters as indicated by the 'N\_PARAM' and 'TDIM15' keywords. Rows and columns of fixed parameters (i.e.: those that have been frozen at a particular value during the fit) are set to zero in the matrix, as reconstructed by transforming the vector into an  $n \times n$  matrix. Finally, the reduced 'goodness-of-fit' test statistic value is given in the 'REDCHSQ' column, as well as the reduced figure of merit. The reduced values of these statistics are computed by dividing the actual statistic by the number of degrees of freedom, stored in 'CHSQDOF'. These names are historical, since *rmfit* now allows both  $\chi^2$  and  $-2 \log$  likelihood fitting. The name of the figure of merit used in the fitting process is provided by the 'STATISTIC' keyword; which is the 'Castor C-STAT' function, in the example.

## REFERENCES

- Amati, L., et al. 2002, *A&A*, 390, 81
- Band, D. L., et al. 1993, *ApJ*, 413, 281
- Baumgartner, W. H. et al. 2008, *GCN Circular* 8330
- Bissaldi, E., et al. 2009, *Exp. Astron.*, 24, 47
- Briggs, M. S., et al. 1999, *ApJ*, 524, 82
- Case, G. L., et al. 2011, *ApJ*, 729, 105
- Cash, W. 1979, *ApJ*, 228, 939
- Ghirlanda, G., Ghisellini, G., & Lazzati, D. 2004, *ApJ*, 616, 331
- Goldstein, A., in prep.
- Guiriec, S., et al. 2010, *ApJ*, 725, 225
- Harmon, B. A., et al. 2002, *ApJS*, 138, 149
- Hoover, A. S., et al. 2008, *AIP Conf. Proc.* 1000, *Gamma-Ray Bursts 2007: Proceedings of the Santa Fe Conference*, ed. M. Galassi, D. Palmer, & E. Fenimore, 565
- Hoover, A., Kippen, M., & Wallace, M. 2010, *General Response Simulation System (GRESS) Software User's Guide*, Document GRESS-SUG-001-21 (Los Alamos, NM: LANL), <http://public.lanl.gov/mkippen/gress/>
- Israel, G. L., et al. 2008, *ApJ*, 685, 2
- Kaneko, Y., Preece, R. D., Briggs, M. S., Paciasas, W. S., Meegan, C. A., & Band, D. L. 2006, *ApJS*, 166, 298
- Kouveliotou, C., Meegan, C. A., Fishman, G. J., Bhat, N. P., Briggs, M. S., Koshut, T. M., Paciasas, W. S., & Pendleton, G. N. 1993, *ApJ*, 413, L101
- Lebrun, F., et al. 2003, *A&A*, 411, L141
- Lee, H. K., Wijers, R. A. M. J., & Brown, G. E. 2000, *Phys. Rep.*, 325, 83
- Lin, L. et al. 2011, accepted to *ApJ*, arxiv: 1107.2121v1
- Lloyd, N. M., Petrosian, V., & Mallozzi, R. S. 2000, *ApJ*, 534, 227
- Mallozzi, R. S., Paciasas, W. S., Pendleton, G. N., Briggs, M. S., Preece, R. D., Meegan, C. A., & Fishman, G. J. 1995, *A&A*, 454, 597
- Meegan, C. A., et al. 2009, *ApJ*, 702, 791
- Mereghetti, S. 2008, *A&A Rev.*, 15, 4
- Mitrofanov, I. G., et al. 1999, *ApJ*, 522, 1069
- Nava, L., Ghirlanda, G., Ghisellini, G., & Celotti, A. 2011, *A&A*, 530, A21
- Preece, R. S., et al. 1998, *ApJ*, 496, 849
- Preece, R. D., Briggs, M. S., Giblin, T. W., Mallozzi, R. S., Pendleton, G. F., & Paciasas, W. S. 2002, *ApJ*, 581, 1248
- Rees, M. J. & Meszaros, P. 1992, *MNRAS*, 258, 41P
- Ryde, F., 1999, *Astro. Lett. and Comm.*, 39, 281
- Sari, R., Piran, T., & Narayan, R. 1998, *ApJ*, 497, L17
- Tierney, D., et al. 2010., *Proc. of Science*, 8th INTEGRAL Workshop: The Restless Gamma-ray Universe, PoS(INTEGRAL 2010)103
- Vedrenne, G., et al. 2003, *A&A*, 411, L63
- von Kienlin, A., et al. 2009, *AIP Conf. Proc.* 1133, *Gamma-ray Bursts: Sixth Huntsville Symposium*, ed. C. A. Meegan, C. Kouveliotou, & N. Gehrels, 446
- Woods, P. M., & Thompson, C. 2006, *Compact stellar X-ray sources*, 547
- Yonetoku, D., et al. 2004, *ApJ*, 609, 935

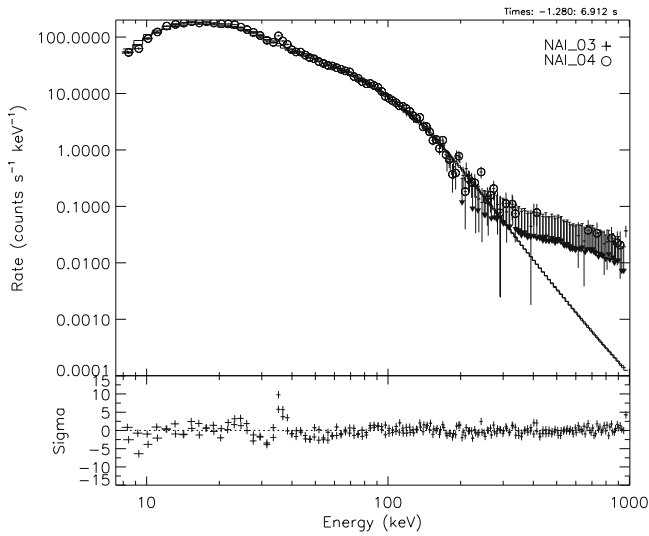


Fig. 1.— Spectrum of GRB 081009 using NaI 3 & 4 with a Band function fit. Note the excess in residuals at the K-edge. The current calibration is inadequate in removing this instrumental effect for many bright bursts.

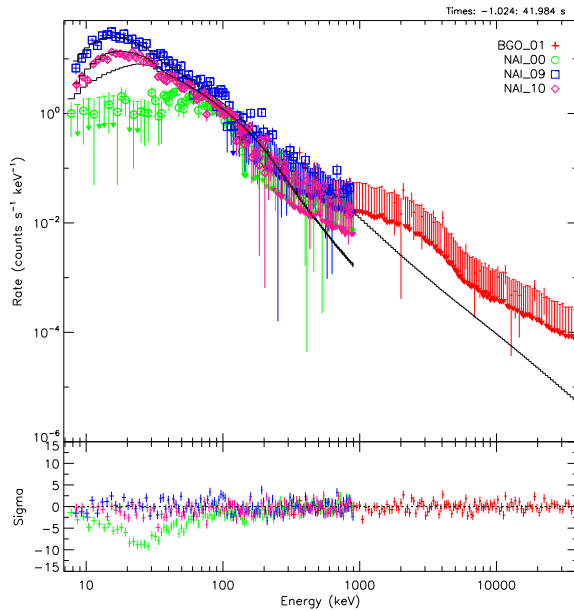
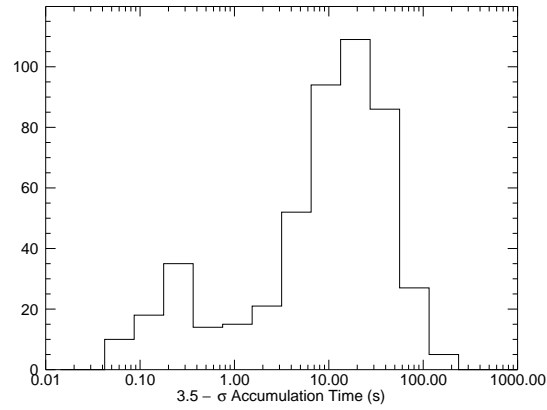
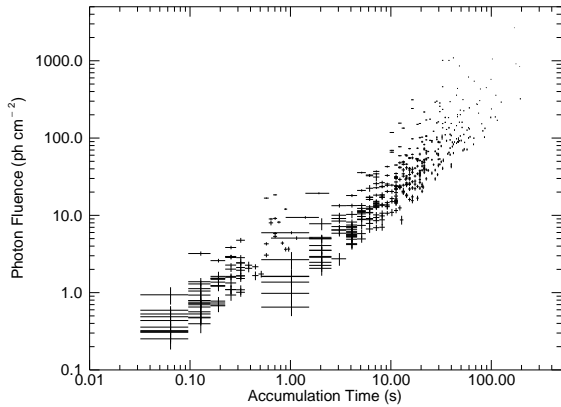


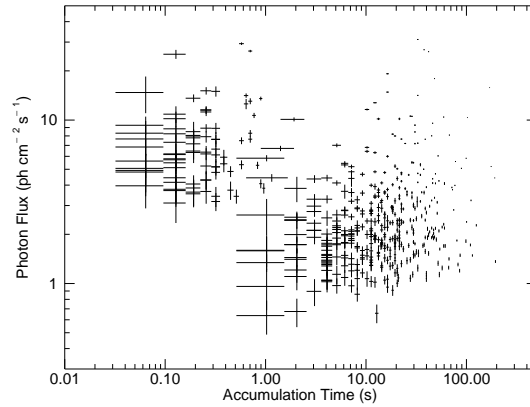
Fig. 2.— Plot of the counts spectrum of GRB 090131 using NaI detectors 0, 9 and 10, and BGO detector 1. Close inspection of the  $\sim 8\text{--}60$  keV range reveals that NaI 0 shows a significant negative trend in residuals and a large deficit in count rate at low energy when compared to the other detectors, indicating a blockage from what is likely the LAT radiator, which is not properly modeled in the DRM.



(a)



(b)



(c)

Fig. 3.— 3(a) is the distribution of the accumulation time based on the  $3.5\sigma$  signal-to-noise selections. Note the similarity to the traditional  $t_{90}$  distribution, with the minimum near 1 second. No other estimation of the duration was factored into the production of the accumulation time. 3(b) and 3(c) show the comparison of the model photon fluence and photon flux to the accumulation time respectively. The fluxes and fluences shown in these figures are from the estimated BEST model fits.

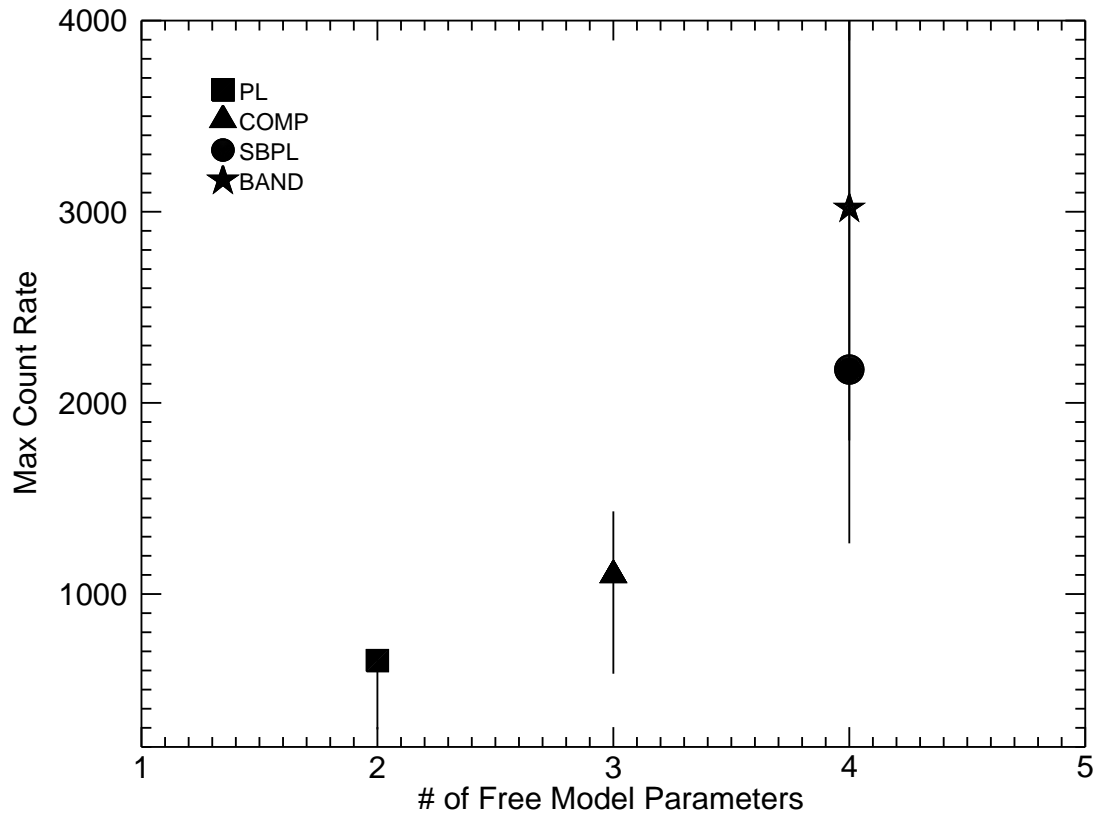
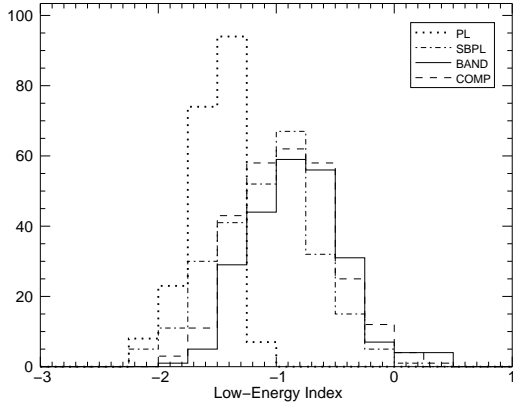
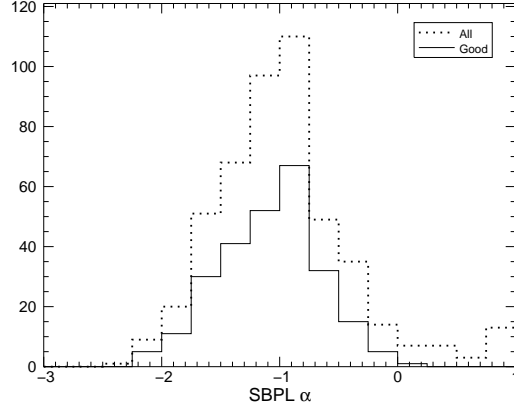


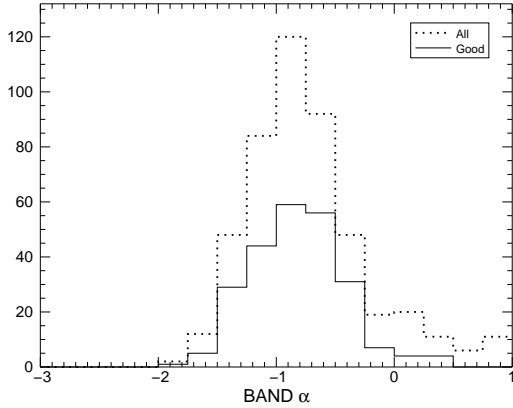
Fig. 4.— Plot of the average maximum background-subtracted count rates (as a proxy for observed intensity) versus the number of degrees of freedom of the best fit model. The count rates in the NaI detectors for each burst was summed, the background subtracted, and the maximum count rate was computed. The best fit model was determined for each burst, and a geometric average was calculated for the maximum count rates of the bursts for each best fit model. The error bars shown are the  $1\sigma$  standard deviations of the distributions of maximum count rates for each best fit model.



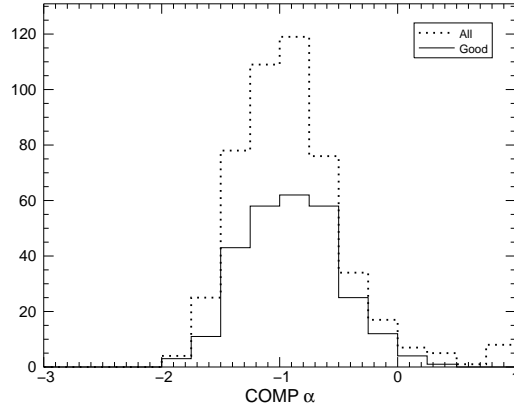
(a)



(b)



(c)



(d)

Fig. 5.— Distributions of the low-energy spectral indices from fluence spectral fits. 5(a) shows the distributions of GOOD parameters and compares to the distribution of PL indices. 5(b)–5(d) display the comparison between the distribution of GOOD parameters and all parameters with no data cuts. The last bin includes values greater than 1.



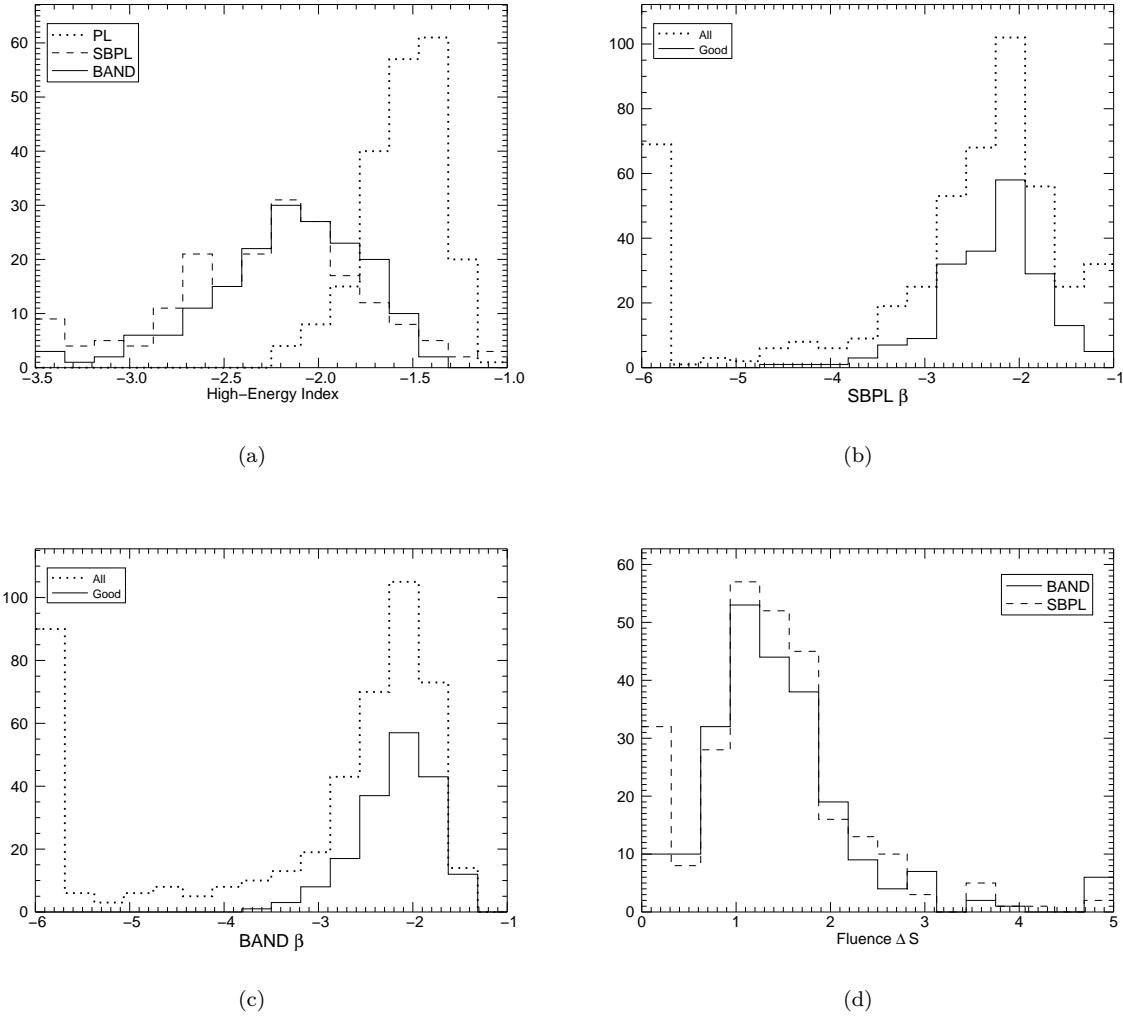
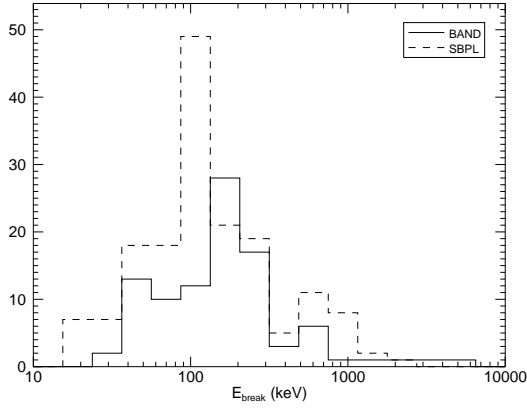
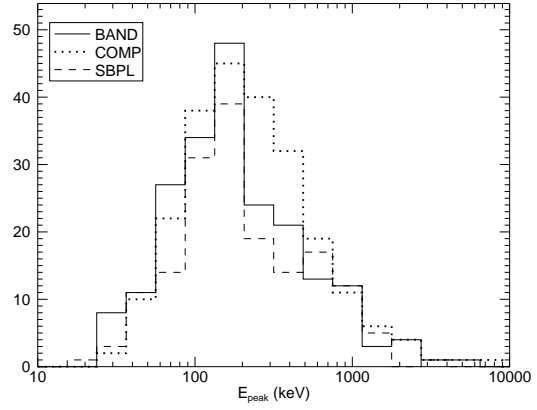


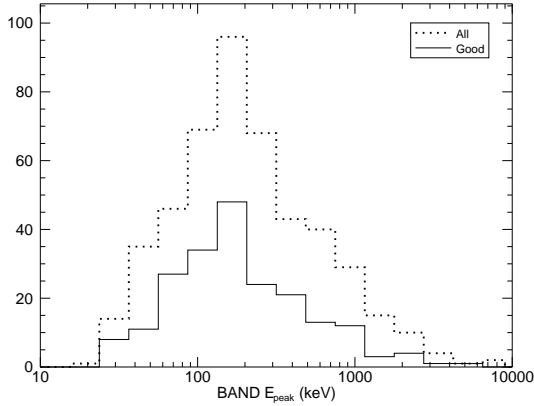
Fig. 6.— 6(a) - 6(c) are distributions of the high-energy spectral indices from fluence spectral fits. 6(a) shows the distributions of GOOD parameters and compares to the distribution of PL indices. 6(b) and 6(c) display the comparison between the distribution of GOOD parameters and all parameters with no data cuts. The first bins include values less than -6 and the last bins includes values greater than -1. 6(d) shows the distribution of the difference between the low- and high-energy indices. The first bin contains values less than 0, indicating that the centroid value of alpha is steeper than the centroid value of beta.



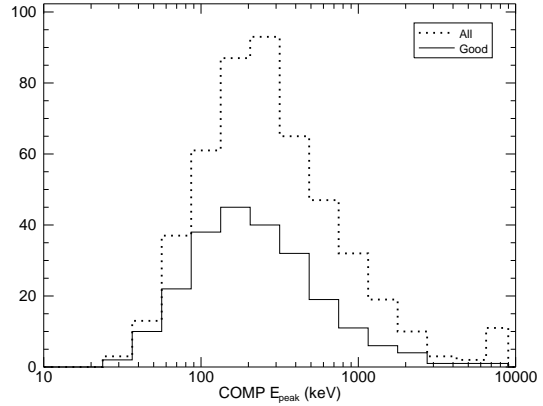
(a)



(b)



(c)



(d)

Fig. 7.— Distributions of  $E_{break}$  and  $E_{peak}$  from fluence spectral fits. 7(a) displays the comparison between the distribution of GOOD  $E_{break}$  and  $E_{break}$  with no data cuts. 7(b) shows the distributions of GOOD  $E_{peak}$  for BAND, SBPL, and COMP. 7(c) and 7(d) display the comparison between the distribution of GOOD parameters and all parameters with no data cuts.

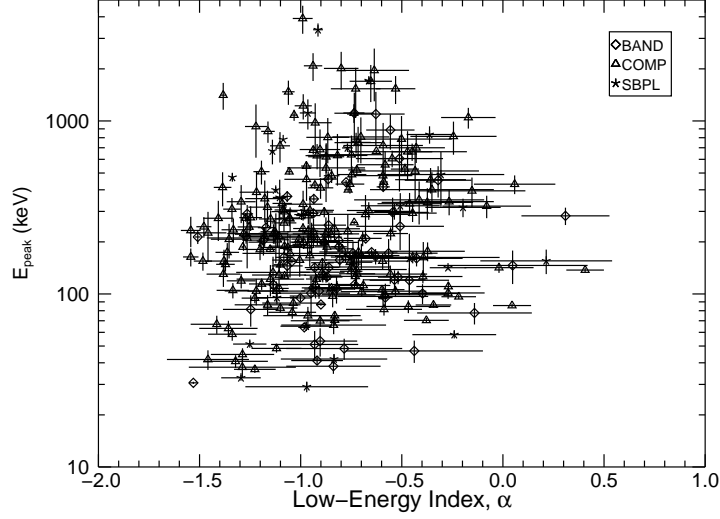


Fig. 8.— Comparison of the low-energy index and  $E_{peak}$  for three models from the fluence spectral fits. This comparison reveals a correlation between the  $E_{peak}$  energy and the uncertainty on the low-energy index: generally a lower energy  $E_{peak}$  tends to result in a less constrained low-energy index.

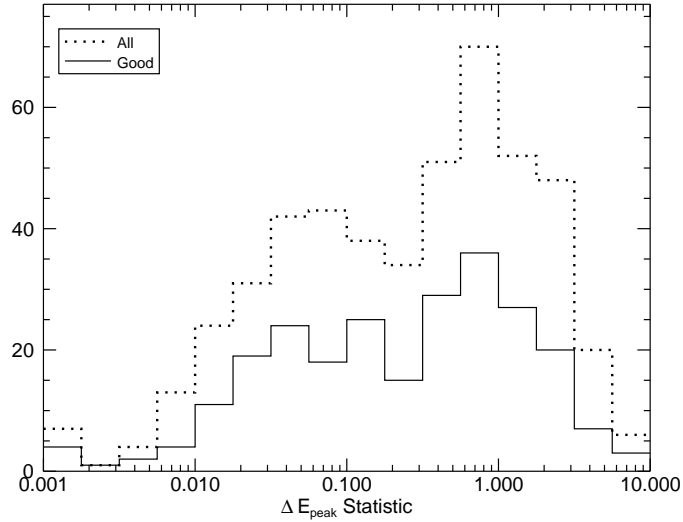
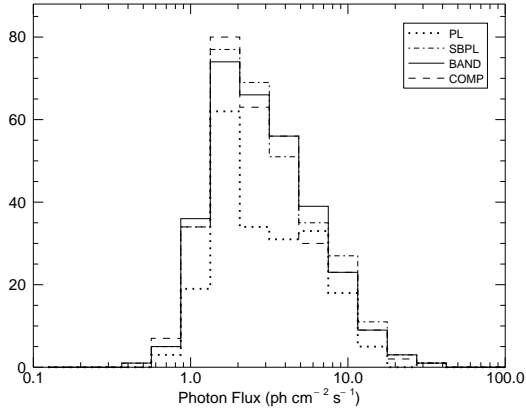
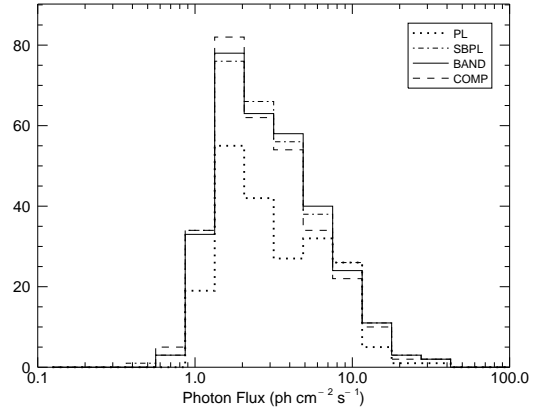


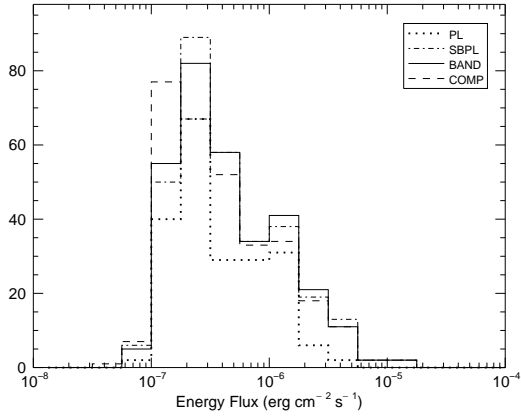
Fig. 9.— Distribution of the  $\Delta E_{peak}$  statistic for the COMP and BAND models from fluence spectral fits. A value less than 1 indicates the  $E_{peak}$  values are within errors, while a value larger than 1 indicates the  $E_{peak}$  values are not within errors.



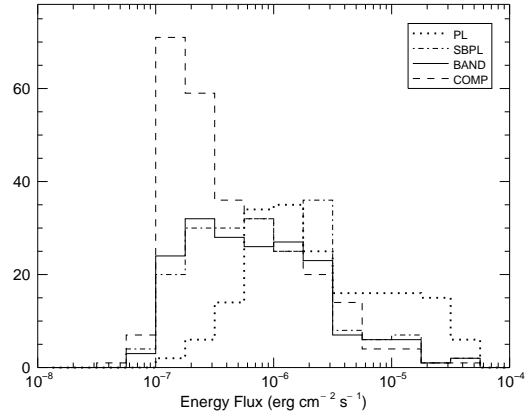
(a)



(b)

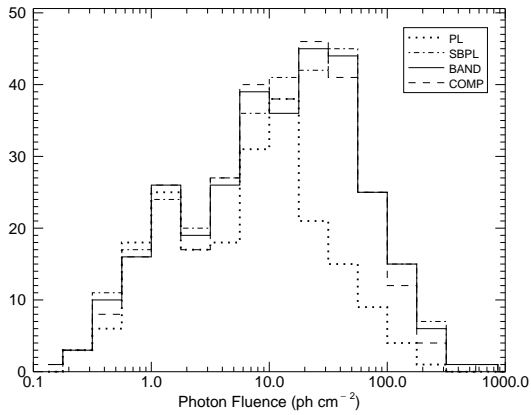


(c)

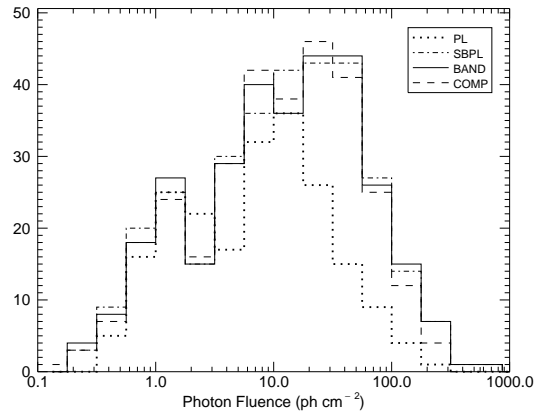


(d)

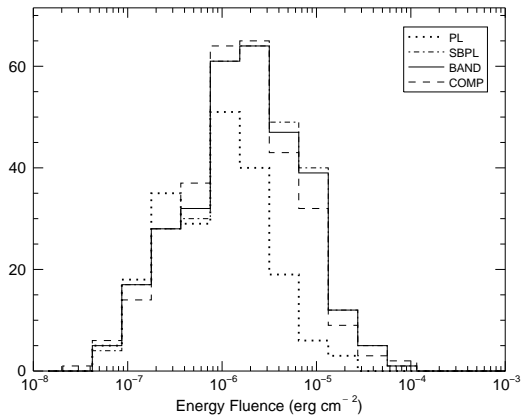
Fig. 10.— Distributions of photon and energy flux from fluence spectral fits. 10(a) and 10(c) display the flux distributions for the 8 keV–1 MeV band. 10(b) and 10(d) display the flux distributions for the 8 keV–40 MeV band. Note that the plotted distributions contain the flux on two different timescales: 1024 ms and 64 ms.



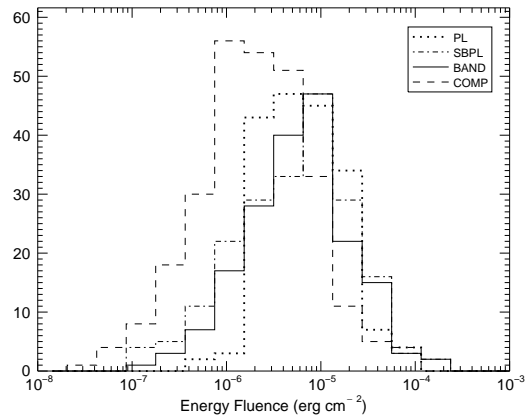
(a)



(b)



(c)



(d)

Fig. 11.— Distributions of photon and energy fluence. 11(a) and 11(c) display the fluence distributions from the 8 keV–1 MeV band. 11(b) and 11(d) display the fluence distributions for the 8 keV–40 MeV band.

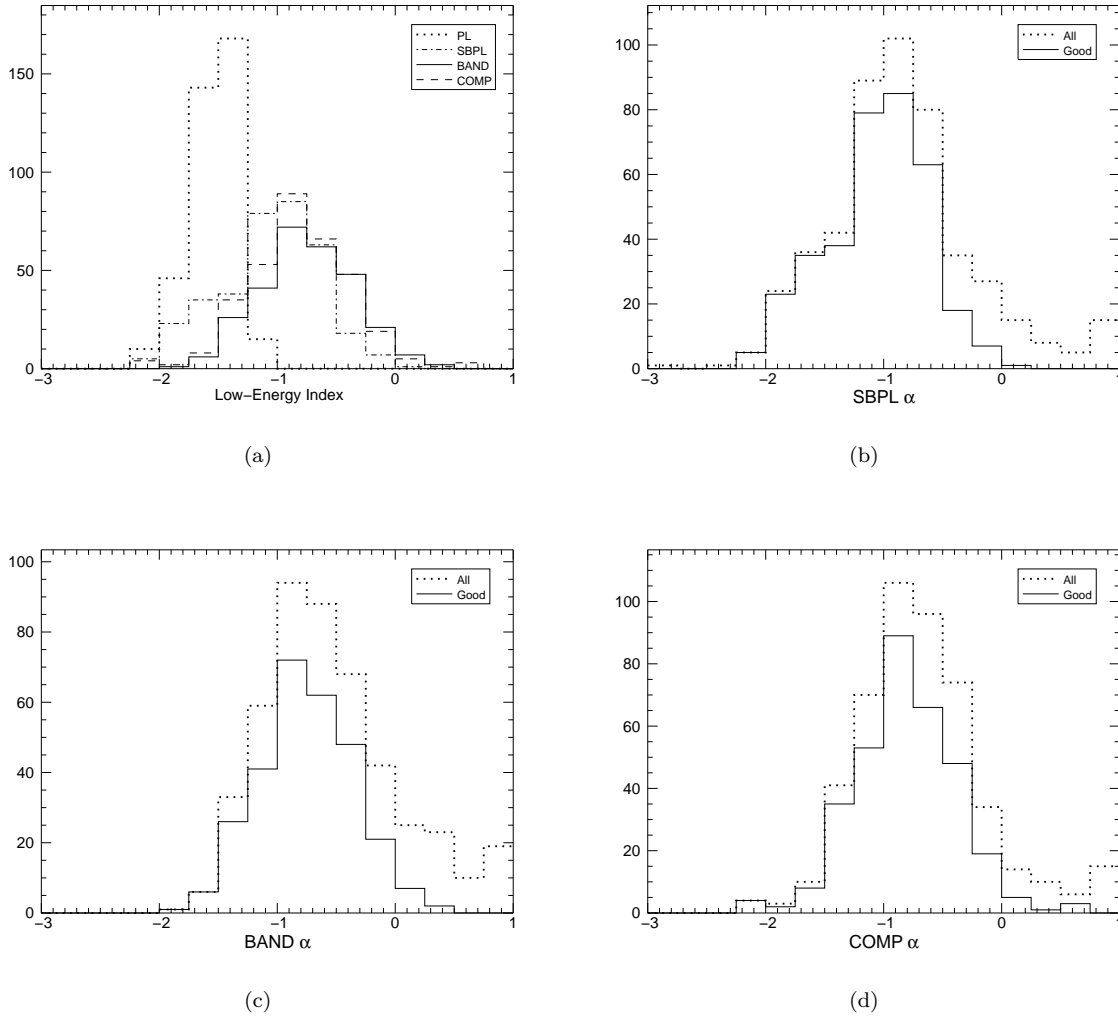


Fig. 12.— Distributions of the low-energy spectral indices from peak flux spectral fits. 12(a) shows the distributions of GOOD parameters and compares to the distribution of PL indices. 12(b)–12(d) display the comparison between the distribution of GOOD parameters and all parameters with no data cuts. The last bin includes values greater than 1.

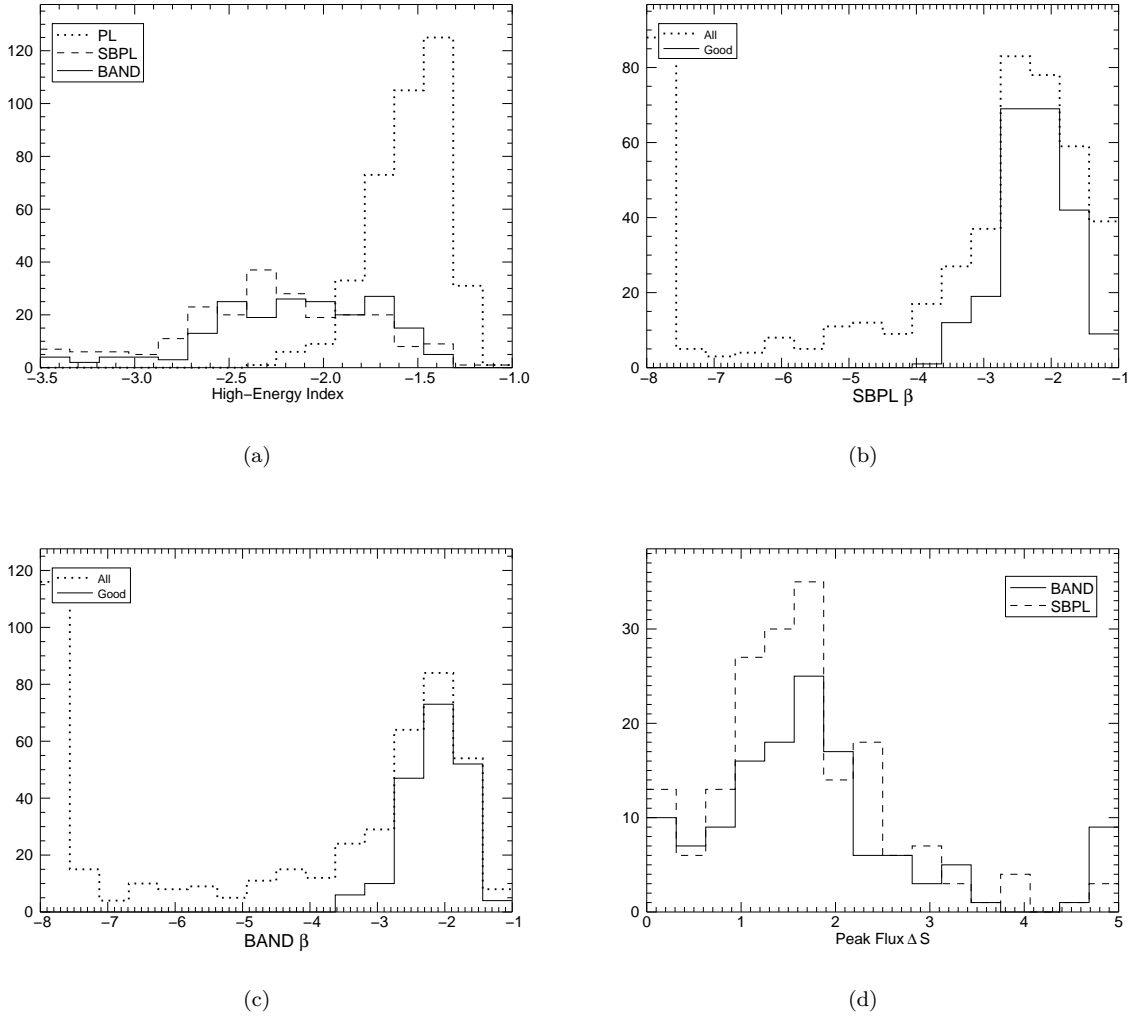


Fig. 13.— 13(a) - 13(c) are distributions of the high-energy spectral indices from peak flux spectral fits. 13(a) shows the distributions of GOOD parameters and compares to the distribution of PL indices. 13(b) and 13(c) display the comparison between the distribution of GOOD parameters and all parameters with no data cuts. The first bins include values less than -6 and the last bins includes values greater than -1. 13(d) shows the difference between the low- and high-energy indices. The first bin contains values less than 0, indicating that the centroid value of alpha is steeper than the centroid value of beta.

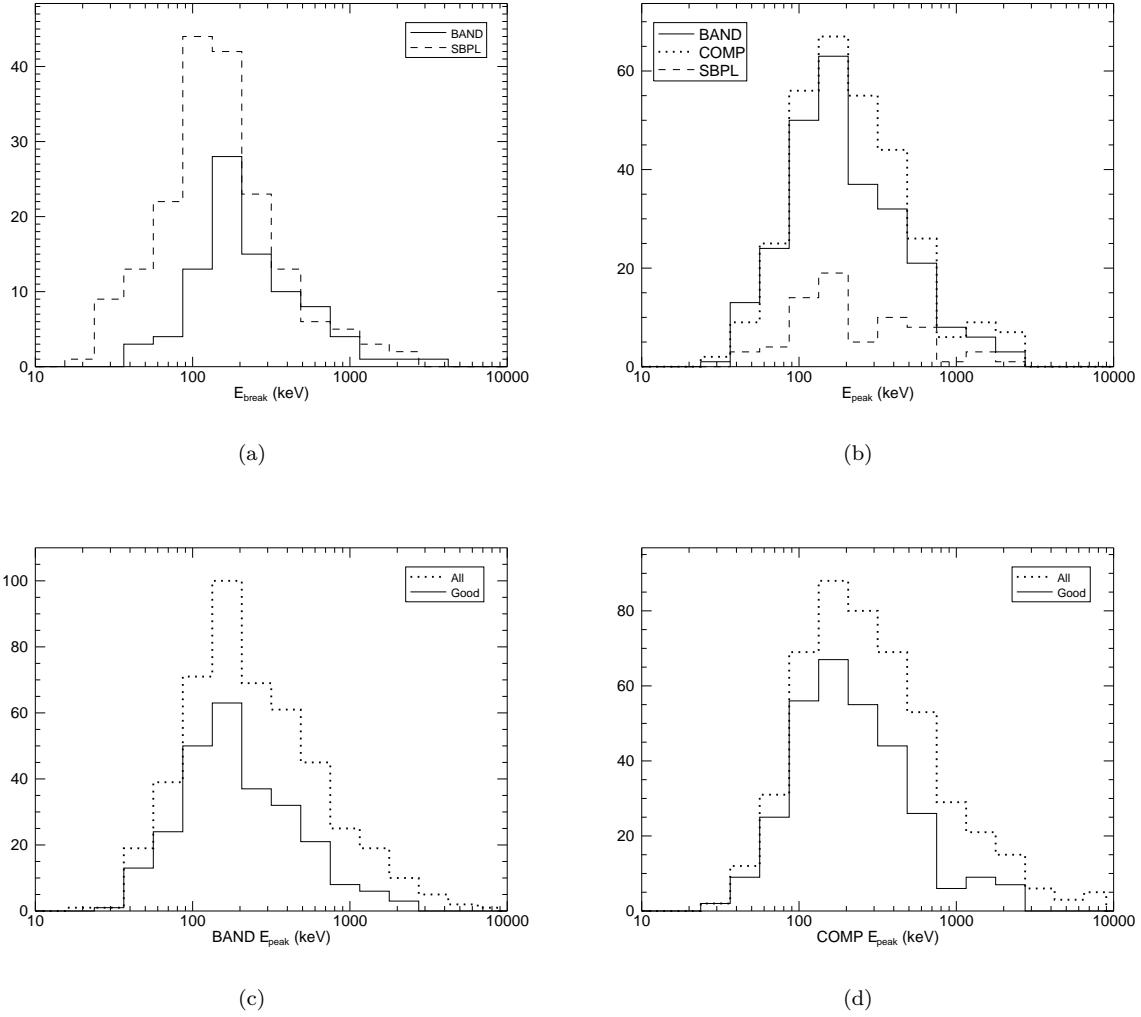


Fig. 14.— Distributions of  $E_{break}$  and  $E_{peak}$  from peak flux spectral fits. 14(a) displays the comparison between the distribution of GOOD  $E_{break}$  and  $E_{break}$  with no data cuts. 14(b) shows the distributions of GOOD  $E_{peak}$  for BAND, SBPL, and COMP. 14(c) and 14(d) display the comparison between the distribution of GOOD parameters and all parameters with no data cuts.



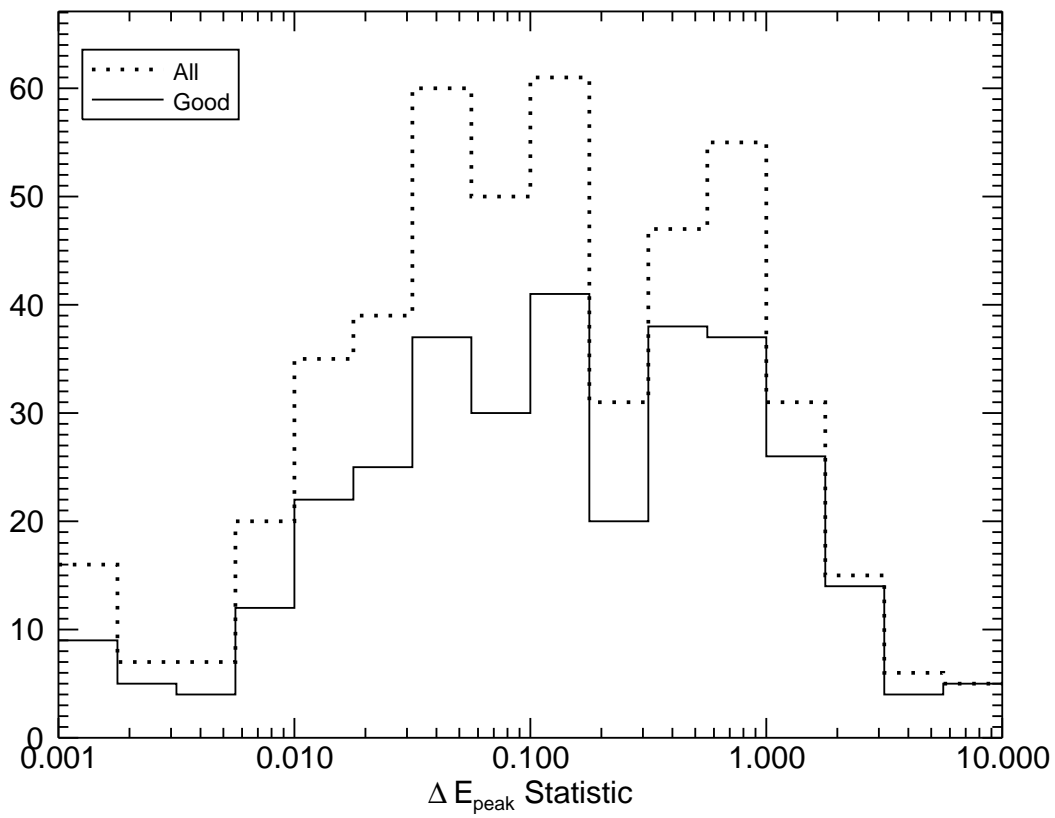


Fig. 15.— Distribution of the  $\Delta E_{peak}$  statistic for the COMP and BAND models from peak flux spectral fits. A value less than 1 indicates the  $E_{peak}$  values are within errors, while a value larger than 1 indicates the  $E_{peak}$  values are not within errors.

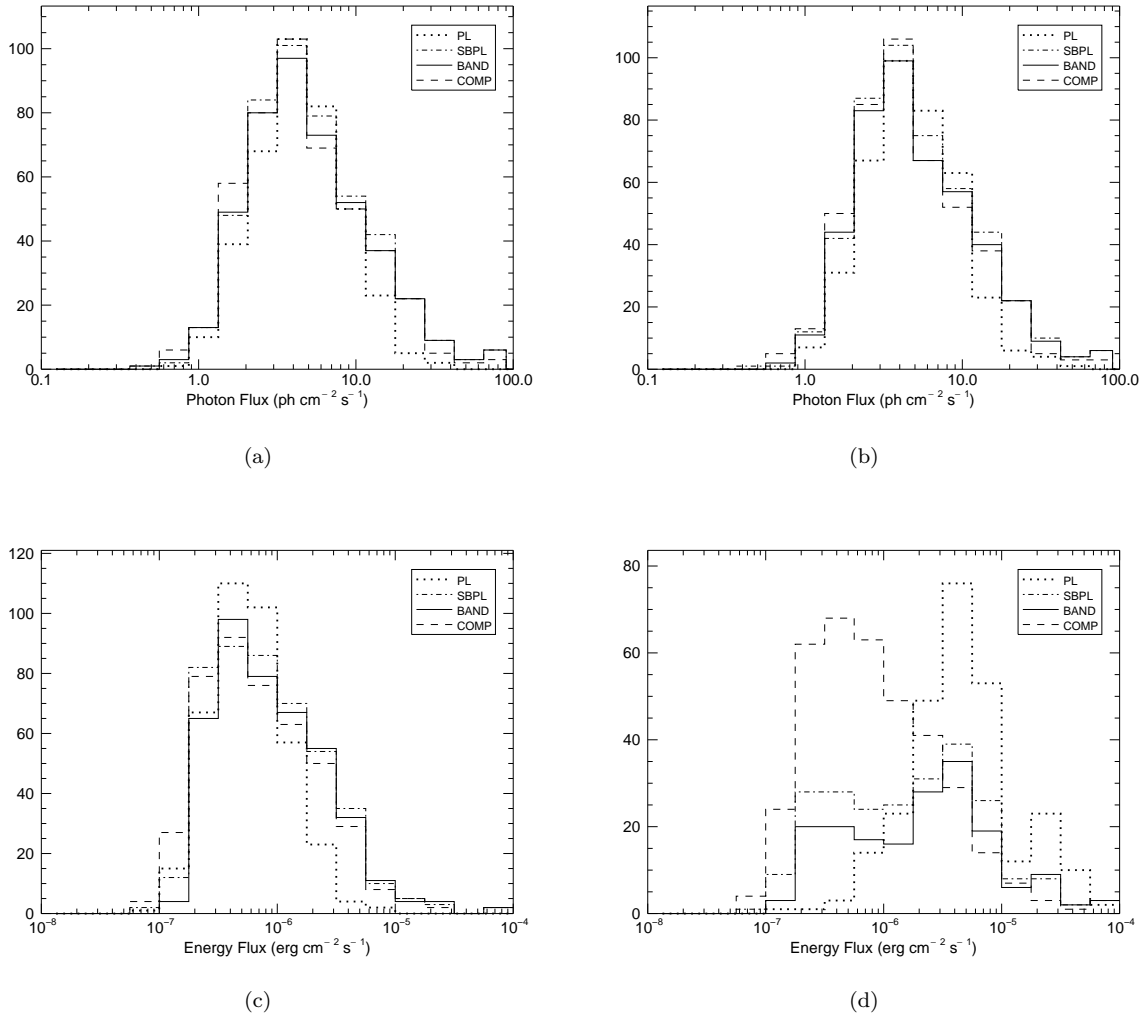


Fig. 16.— Distributions of photon and energy flux from peak flux spectral fits. 16(a) and 16(c) display the flux distributions for the 8 keV–1 MeV band. 16(b) and 16(d) display the flux distributions for the 8 keV–40 MeV band. Note that the plotted distributions contain the flux on two different timescales: 1024 ms and 64 ms.

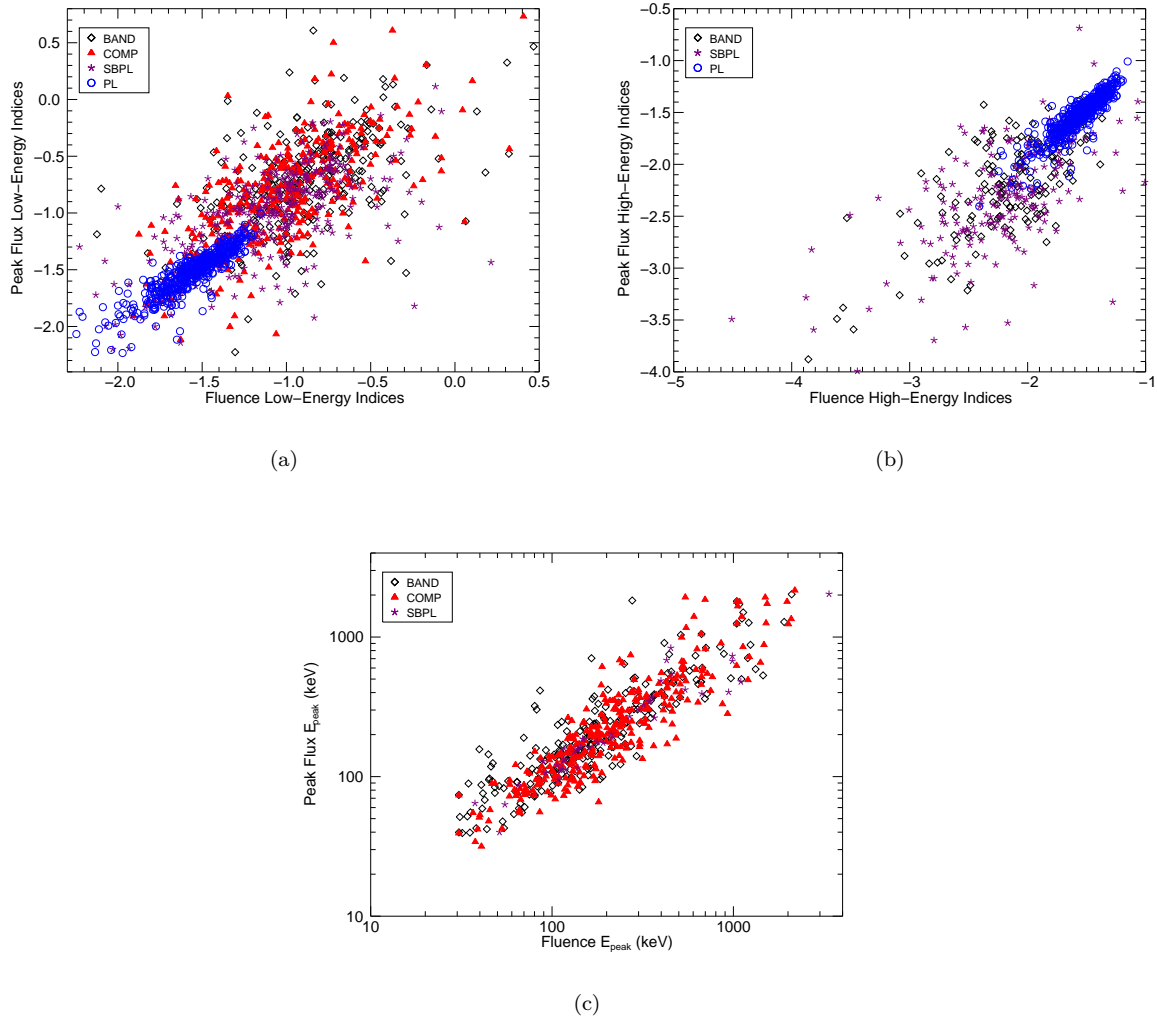


Fig. 17.— Peak flux spectral parameters as a function of the fluence spectral parameters. For all three parameters there is evidence for a strong correlation between the parameters found for the fluence spectra and those for the peak flux spectra. Note that the PL index is shown in both 17(a) and 17(b) for comparison.

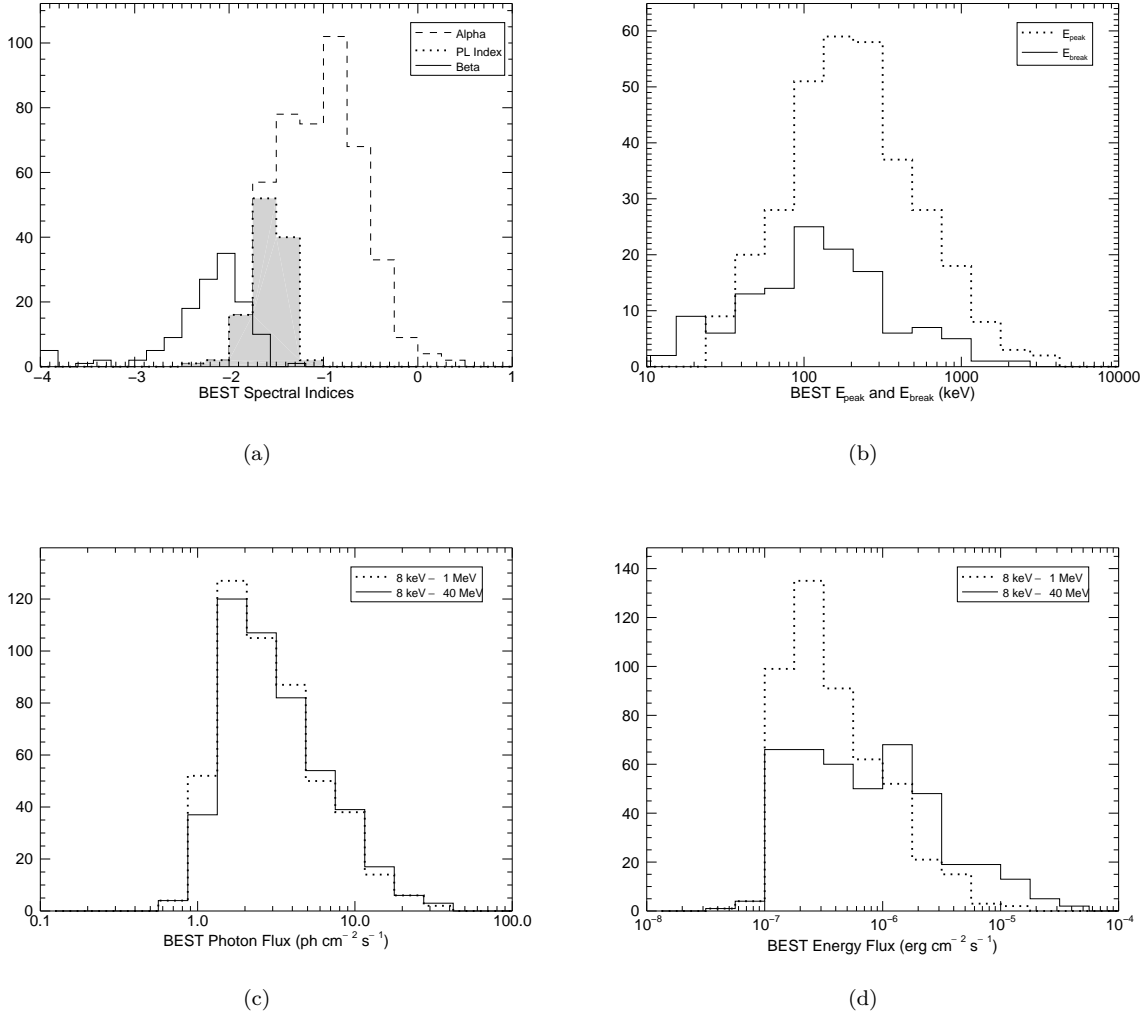


Fig. 18.— Distributions of the BEST spectral parameters for the fluence spectra. 18(a) displays the selection of best low-energy and high-energy spectral indices. The shaded distribution depicts the location of the distribution of the PL index. 18(b) shows the selection of the best  $E_{peak}$  and  $E_{break}$ . 18(c) and 18(d) show the selection of the best photon flux and energy flux respectively.

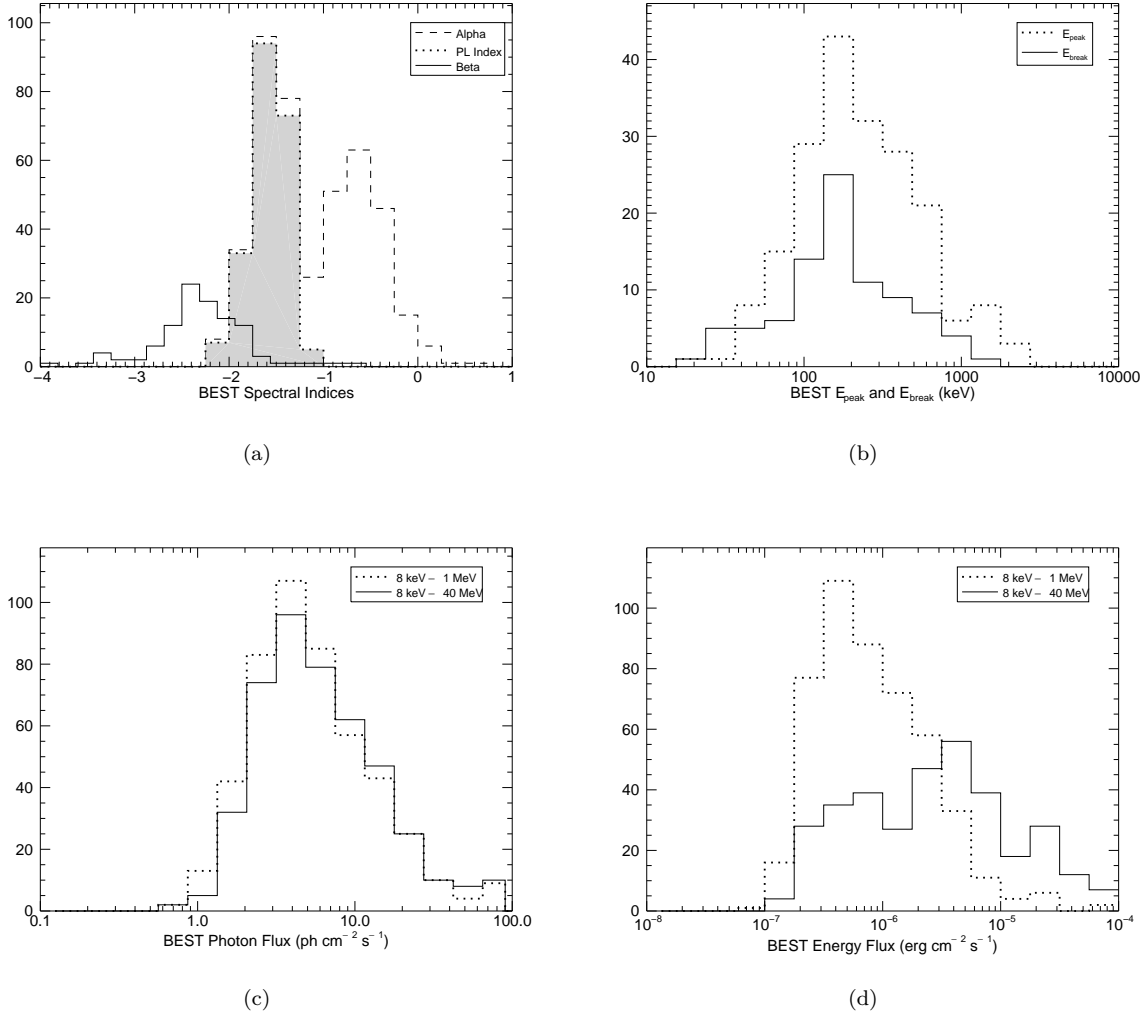
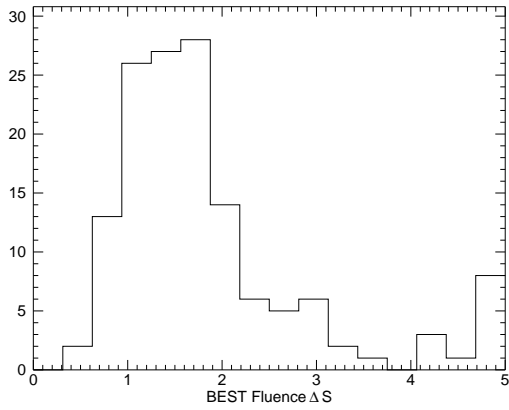
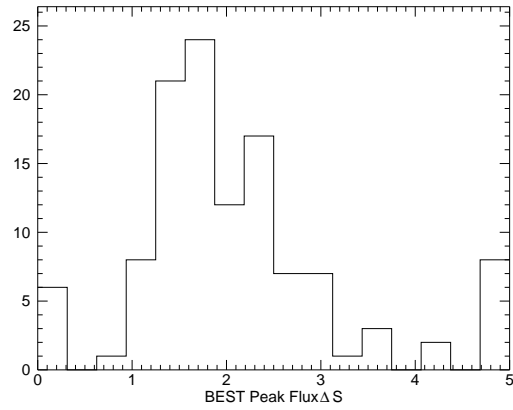


Fig. 19.— Distributions of the BEST spectral parameters for the peak flux spectra. 19(a) displays the selection of best low-energy and high-energy spectral indices. The shaded distribution depicts the location of the distribution of the PL index. 19(b) shows the selection of the best  $E_{peak}$  and  $E_{break}$ . 19(c) and 19(d) show the selection of the best photon flux and energy flux respectively.



(a)



(b)

Fig. 20.— Distributions of the difference between the BEST low- and high-energy spectral indices. The first bin contains values less than 0, indicating that the centroid value of alpha is steeper than the centroid value of beta.

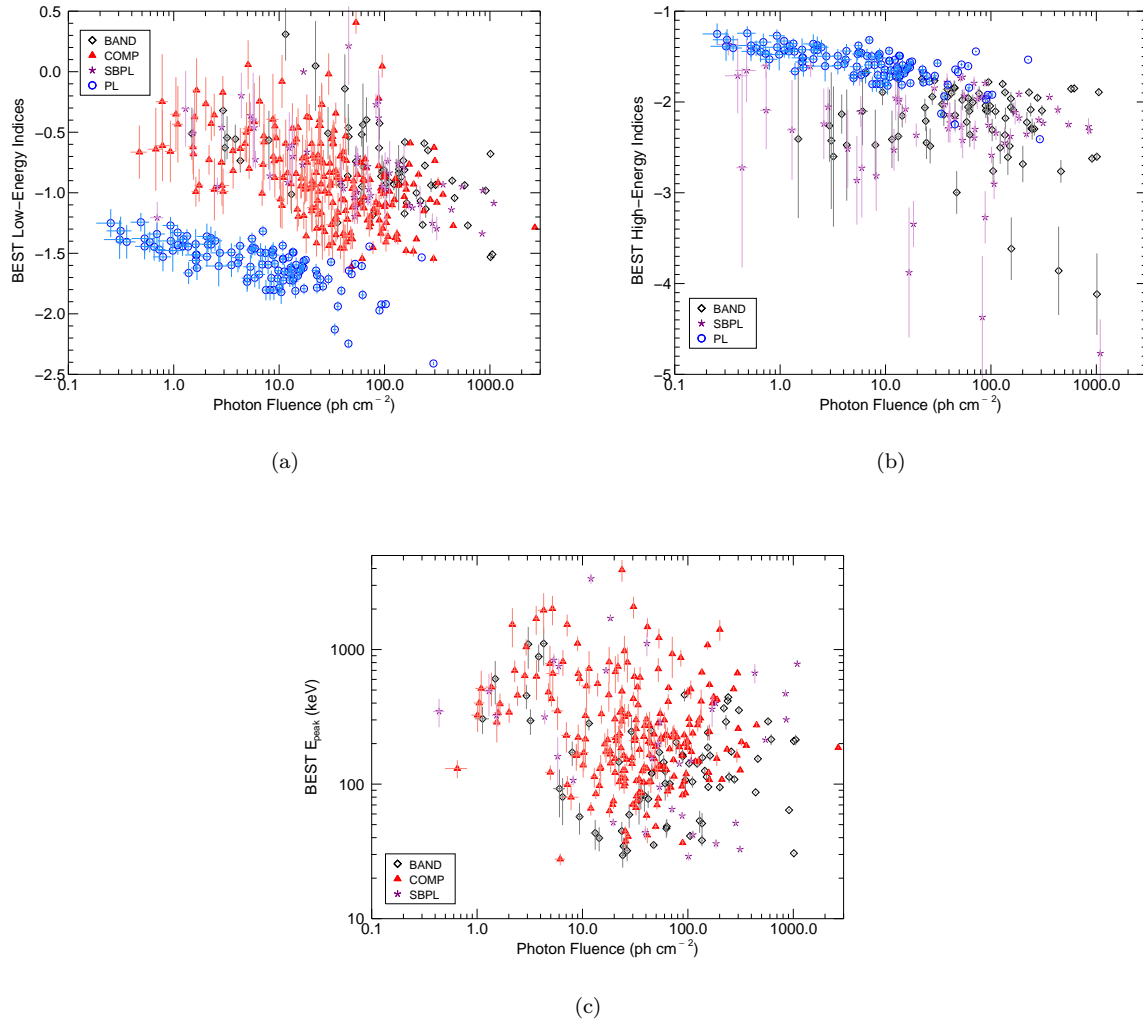


Fig. 21.— BEST fluence spectral parameters as a function of the model photon fluence. Note that the PL index is shown in both 21(a) and 21(b) for comparison.

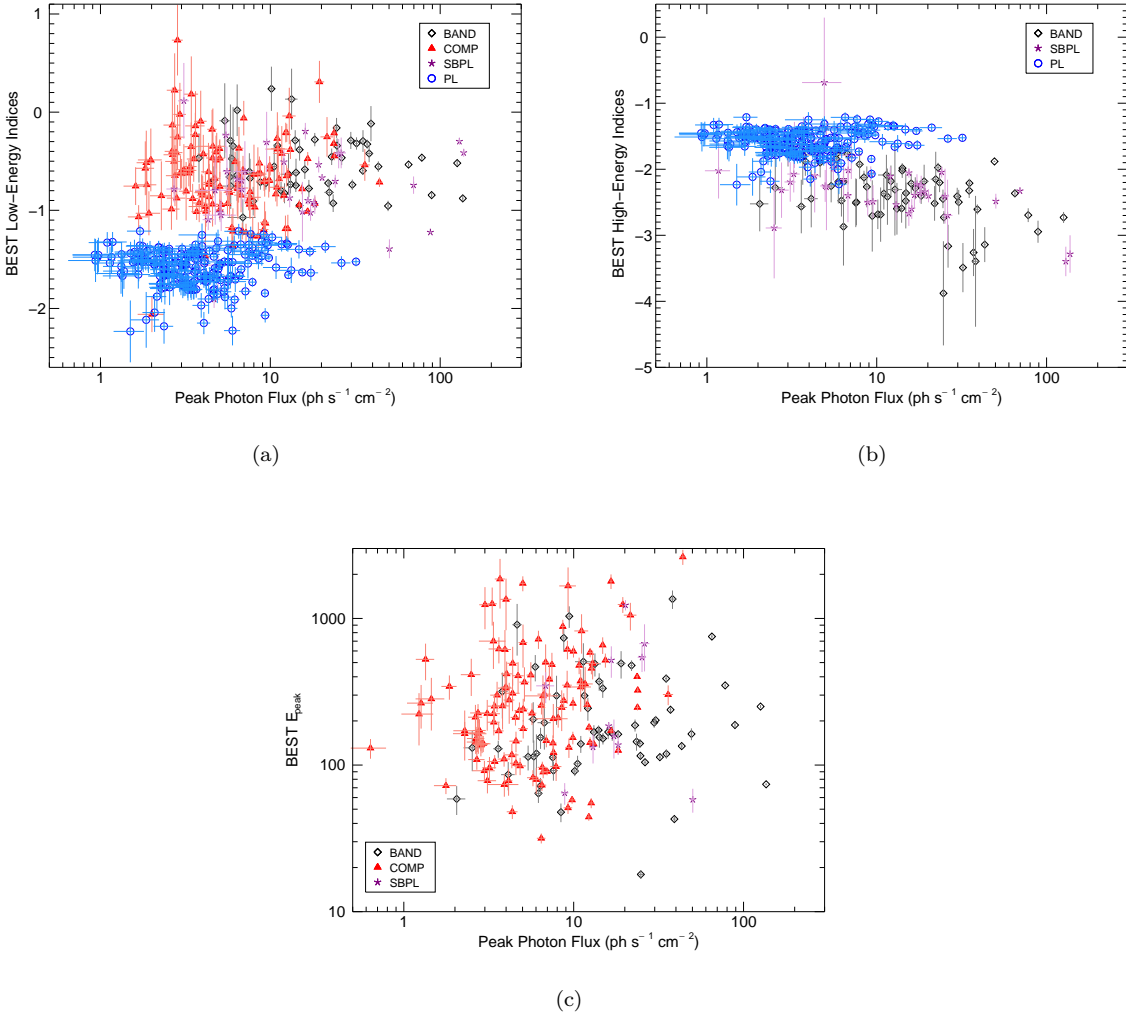


Fig. 22.— BEST flux spectral parameters as a function of the model peak photon flux. Note that the PL index is shown in both 22(a) and 22(b) for comparison.



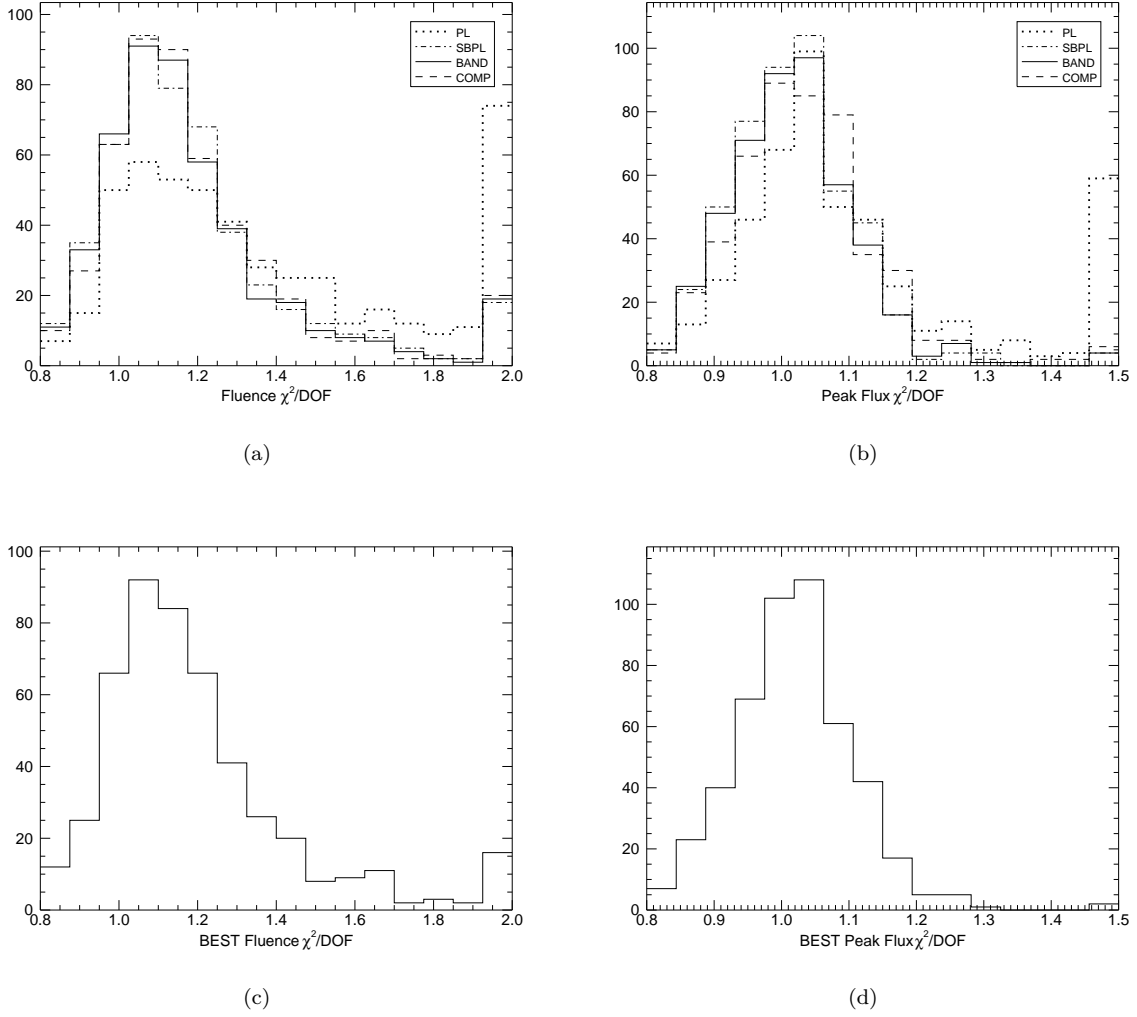


Fig. 23.— Distributions of the reduced  $\chi^2$  for each model. 23(a) and 23(b) are distributions of the reduced  $\chi^2$  for each model for each burst. Note that these distributions include all fits, including unconstrained fits. 23(c) and 23(d) show the distribution of BEST reduced  $\chi^2$  values. The first and last bins in all distributions contain overflow values. Note that the peak of the distributions are slightly larger than 1.

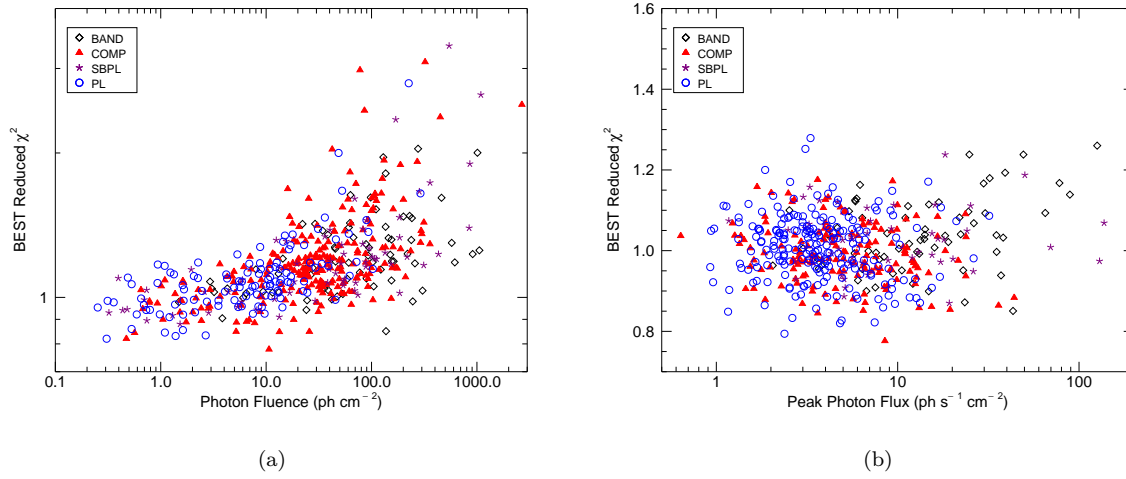


Fig. 24.— 24(a) Reduced  $\chi^2$  as a function of the model photon fluence. 24(b) Reduced  $\chi^2$  as a function of the model peak photon flux.

TABLE 1  
BEST GRB MODELS

PL	SBPL	BAND	COMP
<b>Fluence Spectra</b>			
112 (23%)	68 (14%)	75 (15%)	232 (48%)
<b>Peak Flux Spectra</b>			
213 (44%)	51 (10%)	69 (14%)	154 (32%)

TABLE 2  
SAMPLE MEAN AND STANDARD DEVIATION OF THE PARAMETER DISTRIBUTIONS

Model	Low-Energy Index	High-Energy Index	$E_{\text{peak}}$ (keV)	$E_{\text{break}}$ (keV)	Photon Flux ( $\text{ph s}^{-1} \text{cm}^{-2}$ )	Energy Flux ( $10^{-7} \text{erg s}^{-1} \text{cm}^{-2}$ )
<b>Fluence Spectra</b>						
PL	$-1.54^{+0.18}_{-0.25}$	-	-	-	$2.93^{+3.49}_{-1.36}$	$3.96^{+7.72}_{-1.97}$
COMP	$-0.90^{+0.42}_{-0.38}$	-	$223.75^{+483.80}_{-123.80}$	-	$2.82^{+3.49}_{-1.34}$	$4.01^{+10.54}_{-2.34}$
SBPL	$-1.08^{+0.40}_{-0.46}$	$-2.29^{+0.47}_{-0.65}$	$221.42^{+432.04}_{-129.12}$	$129.74^{+290.08}_{-74.39}$	$2.93^{+3.78}_{-1.54}$	$4.48^{+11.4}_{-1.96}$
BAND	$-0.82^{+0.42}_{-0.38}$	$-2.17^{+0.36}_{-0.47}$	$185.58^{+428.94}_{-81.01}$	$175.50^{+664.50}_{-100.64}$	$2.92^{+3.77}_{-1.39}$	$4.48^{+11.05}_{-2.57}$
BEST	$-1.05^{+0.44}_{-0.45}$	$-2.25^{+0.34}_{-0.73}$	$204.75^{+359.36}_{-121.07}$	$122.71^{+240.41}_{-80.36}$	$2.92^{+3.96}_{-1.31}$	$4.03^{+9.38}_{-2.13}$
<b>Peak Flux Spectra</b>						
PL	$-1.54^{+0.16}_{-0.24}$	-	-	-	$4.34^{+4.33}_{-2.04}$	$5.85^{+7.08}_{-2.91}$
COMP	$-0.81^{+0.44}_{-0.43}$	-	$215.03^{+340.3}_{-113.00}$	-	$4.67^{+7.84}_{-2.45}$	$7.29^{+19.52}_{-4.5}$
SBPL	$-1.05^{+0.38}_{-0.49}$	$-2.27^{+0.48}_{-0.53}$	$217.88^{+395.38}_{-111.72}$	$147.16^{+243.46}_{-80.94}$	$5.09^{+9.18}_{-2.68}$	$8.33^{+21.87}_{-5.00}$
BAND	$-0.75^{+0.41}_{-0.40}$	$-2.16^{+0.40}_{-0.50}$	$194.49^{+313.39}_{-100.38}$	$372.96^{+5086.2}_{-230.02}$	$5.04^{+9.09}_{-2.70}$	$8.91^{+22.34}_{-5.28}$
BEST	$-1.12^{+0.61}_{-0.50}$	$-2.27^{+0.44}_{-0.50}$	$223.12^{+351.55}_{-125.92}$	$172.16^{+253.56}_{-100.49}$	$5.39^{+10.18}_{-2.87}$	$8.35^{+22.61}_{-4.98}$

TABLE 3  
COMPARISON OF THE SAMPLE MEAN AND STANDARD DEVIATION FROM DIFFERENT CATALOGS

Dataset	Low-Energy Index	High-Energy Index	$E_{\text{peak}}$ (keV)	$E_{\text{break}}$ (keV)	Photon Flux ( $\text{ph s}^{-1} \text{cm}^{-2}$ )	Energy Flux ( $10^{-7} \text{erg s}^{-1} \text{cm}^{-2}$ )
<b>Fluence</b>						
This Catalog BEST	$-1.05^{+0.44}_{-0.45}$	$-2.25^{+0.34}_{-0.73}$	$205^{+359}_{-121}$	$123^{+240}_{-80.4}$	$2.92^{+3.96}_{-1.31}$	$4.03^{+9.38}_{-2.13}$
Nava et al. (2011)	$-1.02^{+0.49}_{-0.56}$	$-2.40^{+0.24}_{-0.45}$	$190^{+336}_{-112}$	-	-	$3.05^{+11.5}_{-1.54}$
Kaneko et al. (2006)	$-1.07^{+0.42}_{-0.36}$	$-2.43^{+0.38}_{-0.59}$	$260^{+233}_{-116}$	$203^{+129}_{-80.0}$	$3.32^{+6.01}_{-2.04}$	$8.56^{+16.0}_{-5.47}$
<b>Peak Flux Spectra</b>						
This Catalog BEST	$-1.12^{+0.61}_{-0.50}$	$-2.27^{+0.44}_{-0.50}$	$223^{+352}_{-126}$	$172^{+254}_{-100}$	$5.39^{+10.18}_{-2.87}$	$8.35^{+22.61}_{-4.98}$
Nava et al. (2011)	$-0.55^{+0.42}_{-0.37}$	$-2.37^{+1.42}_{-0.61}$	$241^{+387}_{-138}$	-	-	$14.9^{+53.8}_{-10.7}$